Author/s:
Farzana, F;McConville, M;Renoir, T;Li, S;Nie, S;Tran, H;Hannan, AJ;Hatters, DM;Boughton, BA

Title:
Longitudinal spatial mapping of lipid metabolites reveals pre-symptomatic changes in the hippocampi of Huntington's disease transgenic mice

Date:
2023-01-01

Citation:
Farzana, F., McConville, M., Renoir, T., Li, S., Nie, S., Tran, H., Hannan, A. J., Hatters, D. M. & Boughton, B. A. (2023). Longitudinal spatial mapping of lipid metabolites reveals pre-symptomatic changes in the hippocampi of Huntington's disease transgenic mice. Neurobiology of Disease, 176, https://doi.org/10.1016/j.nbd.2022.105933.

Persistent Link:
https://hdl.handle.net/11343/325360

Neurobiology of Disease 176 (2023) 105933

Contents lists available at ScienceDirect

Neurobiology of Disease

journal homepage: www.elsevier.com/locate/ynbdi

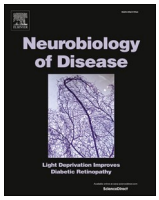

Longitudinal spatial mapping of lipid metabolites reveals pre-symptomatic changes in the hippocampi of Huntington's disease transgenic mice

Farheen Farzana [a,b], Malcolm J. McConville [b,c], Thibault Renoir [a], Shanshan Li [a], Shuai Nie [d], Harvey Tran [a], Anthony J. Hannan [a,*,1], Danny M. Hatters [b,*,1], Berin A. Boughton [e,f,*,1]

[a] Florey Institute of Neuroscience & Mental Health, The University of Melbourne, Victoria 3010, Australia
[b] Department of Biochemistry and Pharmacology, Bio21 Molecular Science and Biotechnology Institute, The University of Melbourne, Victoria 3010, Australia
[c] Metabolomics Australia, The University of Melbourne, Victoria 3010, Australia
[d] Melbourne Mass Spectrometry and Proteomics Facility, Bio21 Molecular Science and Biotechnology Institute, The University of Melbourne, Victoria 3010, Australia
[e] School of Biosciences, The University of Melbourne, Victoria 3010, Australia
[f] Australian National Phenome Centre, Murdoch University, Murdoch 6150, Western Australia, Australia

ARTICLE INFO

Keywords:
Neurodegeneration
Kinetic mass spectrometry imaging (kMSI)
Deuterium labelling
Huntingtin inclusions
Neuronal membrane lipids
In vivo metabolic activity

ABSTRACT

In Huntington's disease (HD), a key pathological feature includes the development of inclusion-bodies of fragments of the mutant huntingtin protein in the neurons of the striatum and hippocampus. To examine the molecular changes associated with inclusion-body formation, we applied MALDI-mass spectrometry imaging and deuterium pulse labelling to determine lipid levels and synthesis rates in the hippocampus of a transgenic mouse model of HD (R6/1 line). The R6/1 HD mice lacked inclusions in the hippocampus at 6 weeks of age (pre-symptomatic), whereas inclusions were pervasive by 16 weeks of age (symptomatic). Hippocampal subfields (CA1, CA3 and DG), which formed the highest density of inclusion formation in the mouse brain showed a reduction in the relative abundance of neuron-enriched lipids that have roles in neurotransmission, synaptic plasticity, neurogenesis, and ER-stress protection. Lipids involved in the adaptive response to ER stress (phosphatidylinositol, phosphatidic acid, and ganglioside classes) displayed increased rates of synthesis in HD mice relative to WT mice at all the ages examined, including prior to the formation of the inclusion bodies. Our findings, therefore, support a role for ER stress occurring pre-symptomatically and potentially contributing to pathological mechanisms underlying HD.

1. Introduction

Huntington's disease (HD) is caused by an expansion of a CAG repeat sequence within exon 1 of the *Huntingtin* gene (Httex1) (MacDonald et al., 1993). The CAG sequence encodes polyglutamine (polyQ), which upon disease-expansion lengths, mediates aggregation of the huntingtin protein and N-terminal fragments into intracellular inclusions (DiFiglia et al., 1997; Scherzinger et al., 1999). The CAG-expanded huntingtin protein and N-terminal fragments containing the polyQ sequence are toxic in a wide range of animal and cell culture models, which suggests that one or more processes directly or indirectly connected to the aggregation mechanism are involved in the disease process (Davies et al., 1997; Lajoie and Snapp, 2010; Takahashi et al., 2008).

Prior work has shown that the risk of cultured rat neurons expressing Httex1 dying is reduced once Httex1 forms inclusions (Arrasate et al., 2004), which has led to the concept that inclusion body formation may be an adaptive response to the toxicity. However, we showed that while soluble huntingtin protein causes elevated rates of apoptosis in an immortalized cell culture model, when inclusions formed the cells display a quiescent metabolic state and die more slowly through a necrotic mechanism (Ramdzan et al., 2017). These results led us to hypothesize that inclusion-body mediated quiescence is an important contributing factor to neurological dysfunction in HD.

To investigate the extent of quiescence in vivo, we sought to examine the state of metabolism in brain tissue with dense formation of huntingtin inclusions using a transgenic mouse model of HD. The R6/1 transgenic mouse model of HD (hereon called HD mice) expresses the human HTT exon 1 under the human huntingtin promoter at near

* Corresponding authors.
E-mail addresses: anthony.hannan@florey.edu (A.J. Hannan), dhatters@unimelb.edu (D.M. Hatters), Berin.boughton@murdoch.edu.au (B.A. Boughton).
[1] Joint senior authors.

https://doi.org/10.1016/j.nbd.2022.105933
Received 26 September 2022; Received in revised form 16 November 2022; Accepted 23 November 2022
Available online 25 November 2022

physiological expression levels (Mangiarini et al., 1996). HD mice display cognitive and affective deficits (Ransome et al., 2012a; Mo et al., 2013) from 8 to 10 weeks of age (both of which are associated with hippocampal dysfunction), motor deficits from around 12 weeks onwards (Rattray et al., 2013). Neuronal death occurs at 20–24 weeks, suggesting that if metabolic quiescence is relevant to the mechanisms of dysfunction, the effects will be maximally present between 8 and 20 weeks (Brooks et al., 2012; Spires et al., 2004).

Matrix Assisted Laser Desorption Ionization–Mass Spectrometry Imaging (MALDI-MSI) is a sensitive method able to spatially track changes in neuronal membrane lipids, which are anticipated to be highly sensitive to changes in metabolism. Moreover, kinetic mass spectrometry imaging (kMSI), which integrates MALDI-MS with stable isotope labelling of tissues over time, aids in the determination of metabolic turnover in a spatiotemporal manner, thus allowing greater insight into the dynamic spatial changes in metabolism (Farzana et al., 2022). The mouse hippocampus is ideal for this goal in that it contains near homogenous populations of neurons, localized to specific sub-fields – Cornu Ammonis (CA) fields (1–3) pyramidal cell layer and the dentate gyrus (DG) granule cell layer that become densely enriched with inclusions as HD mice age (Rattray et al., 2013; Lazic et al., 2004; Cabanas et al., 2020). The hippocampus is also readily distinguished from surrounding brain regions, meaning it is highly amenable for defining a clear boundary for MALDI-MSI and assessing how inclusion formation alters the metabolism using a longitudinal study design.

While HD is widely recognized to most heavily impact the caudate putamen with respect to cell loss, hippocampal-dependent cognitive dysfunction has been found to occur at an early stage in HD patients (Harris et al., 2019), with the onset of cognitive deficits (e.g., impairment of spatial learning and memory) known to precede motor symptoms in HD (Giralt et al., 2012a; Paulsen, 2011; Ravalia et al., 2021). Post-mortem studies have provided evidence for hippocampal volume loss and a widespread neurodegeneration across the hippocampus in the early-mid stages of HD (de la Monte et al., 1988; Rosas et al., 2003). Reduced hippocampal neurogenesis in the dentate gyrus (Lazic et al., 2004; Gil-Mohapel et al., 2011), impaired hippocampal-dependent cognitive functions such as spatial learning and memory, and altered hippocampal synaptic plasticity (Murphy et al., 2000a; Tyebji and Hannan, 2017) have been reported in animal models of HD.

2. Materials and methods

2.1. Animal care

The HD mice (R6/1) were verified by sequencing to have between 135 and 140 CAG repeats in the human *HTT* transgene. The HD mice and wild-type (WT) littermates were generated by crossing F1 hybrid (CBA × C57Bl/6) females and hemizygous HD males. Animals were bred onsite and group-housed (4–5 mice/cage) by genotype in a fully controlled SPF facility (12 h light/dark cycle, temperature (22 °C) and humidity (45%)) at the Florey Institute of Neuroscience and Mental Health. All mice were provided with ad libitum access to food and water. All animal care and experimental procedures were approved by the Florey Institute of Neuroscience and Mental Health Animal Ethics Committee and were conducted by complying with the Australian Code of Practice for the Care and Use of Animals for Scientific Purposes as outlined by the National Health and Medical Research Council of Australia (Ethics number - 17-059-FINMH and 19-019-FINMH).

2.2. Study design

This study was conducted using three cohorts. Cohort 1 was used in time-course experiments for tracking the appearance of inclusion bodies at 6, 8, 10 and 12 weeks of age in WT and HD mice ($n = 3$/group). Cohort 2 (6 and 12 weeks of age), and Cohort 3 (16 weeks of age) ($n = 6$/group, 1:1 male: female), were used for the metabolomics study. Briefly, WT and HD mice were labelled with ^2H_2O following established protocols (Kloehn et al., 2015) at the three age groups examined by injecting a 35 μl/g body weight intraperitoneal (IP) bolus dose of sterile 99.9 atom% deuterium oxide (Sigma-Aldrich) containing 0.9% *v*/v NaCl. This was followed by the inclusion of 9% v/v ^2H_2O in drinking water for eight days to maintain a constant level of 5% v/v ^2H_2O in the body water of mice. An equal number of unlabeled control and HD mice were provided free access to regular drinking water. A total of 110 mice were used in the experimental procedures.

2.3. Tissue processing and immunohistochemistry

To validate the presence of inclusions, mice from Cohort 1 were anesthetized using an IP injection of Lethabarb (325 mg/ml pentobarbitone sodium, Virbac, Peakhurst, NSW, Australia) followed by intracardial perfusion with phosphate buffered saline (PBS) and 4% *w/v* paraformaldehyde (PFA) solution dissolved in PBS (pH 7.4). The collected brain tissue was post-fixed in 4% w/v PFA for 24 h at 4 °C, saturated in 20% w/v sucrose for 48 h at 4 °C or until the tissue sank. It was then frozen in liquid nitrogen-cooled isopentane and stored at −80 °C until further use. The tissue was then mounted on an OCT embedding medium and cryosectioned to collect serial coronal sections (40 μm) spanning the whole of the dorsal hippocampus (Bregma −0.95 mm to 2.53 mm) and stored in a cryo-preservant composed of PBS, 25% v/v ethylene glycol (VWR International, Leuven, Belgium) and 25% v/v glycerol (Chem-Supply, Gilman, SA, Australia) at −20 °C until further use. Free-floating sections were then transferred to net wells submerged in 12-well plates and washed three times in PBS, followed by incubation in hydrogen peroxide (1% *v*/v in PBS). Antigen retrieval was performed by incubating sections in 10 mM sodium citrate buffer (pH 6.0) containing 0.05% v/v Tween 20 (Sigma-Aldrich) for 30 min at 80 °C. Next, the sections were incubated in blocking buffer consisting of 10% v/v normal donkey serum (Merck-Millipore, VIC, Australia) and 0.2% v/v Triton X (Sigma-Aldrich) in PBS for one hour, followed by incubation in mouse EM48 anti-huntingtin protein antibody (MAB5374, Merck-Millipore, Kilsyth, Australia) diluted 1/100 in blocking buffer overnight at 20 °C. The next day, sections were washed three times in PBS and then incubated in biotinylated goat anti-mouse (BA-9200-1.5, Vector Laboratories, Burlingame, CA, USA) diluted 1/200 in blocking buffer for two hours. Finally, the sections were incubated in Vectastain ABC solution (1:100 dilution in PBS, PK-6200, Vector Laboratories, Burlingame, CA) for one hour and colour was developed using 3,3′ Diaminobenzidine (DAB) liquid chromogen kit (1:50 dilution in buffer solution; Dako Australia). The stained sections were then mounted on slides and dried overnight. Dibutyl phthalate polystyrene xylene was used to coverslip the slides and allowed to dry before being visualized using an Olympus BX61 light microscope (Olympus America, Center Valley, PA, USA). Digital images were captured using ×10 and ×40 objective lenses, a Micropublisher 5.0 RTV Camera (Q Imaging, Surrey, BC, Canada) and Image-Pro Plus 6.0 software (Media Cybernetics, Rockville, MD, USA).

2.4. Tissue processing for metabolomics and immunofluorescence

To conduct metabolomics experiments, both unlabeled and ^2H labelled mice from Cohorts 2 and 3 were euthanized at an equivalized eight days post-labelling using cervical dislocation. The excised brain tissues were then hemisectioned on a cold plate. While one brain hemisphere (left) was flash-frozen on liquid nitrogen and reserved for mass spectrometry imaging (MSI), the other matched hemisphere (right) was dissected to obtain the frontal cortex, hippocampus, and striatum which were homogenized, extracted, and examined in detail using LC-MS/MS analysis. The brain regions were immediately snap-frozen in liquid nitrogen (within 3–5 min after brain excision) and stored at −80 °C until further use. The left hemisphere of the brain was mounted on Optimal Cutting Temperature (OCT) embedding medium (Thermo

Fisher Scientific, Waltham, MA, USA) and cryosectioned using a Leica CM1950 cryostat (Leica Microsystems Pty Ltd., VIC, Australia) at −17 °C. Serial coronal sections from 1.42 to −2.48 mm Bregma were obtained at 20 μm thickness and collected in a one in 10 series spaced 200 μm apart, thereby sampling the caudate-putamen and the entire length of the dorsal hippocampus. Sections were thaw mounted by placing a finger on the reverse side of the microscopic glass slides (Menzel-Glaeser Superfrost Ultra Plus, Thermo Fisher Scientific, Waltham, MA, USA). While one hippocampal section was dehydrated in a vacuum desiccator for 15 min and used for MSI measurement, the two consecutive frozen sections were used for staining purposes. To confirm the integrity of the tissue and obtain anatomical information, the second consecutive hippocampal section was processed for hematoxylin and eosin (H&E) staining, while the third section was subjected to EM48 immunofluorescene for the visualization of huntingtin inclusions. High-resolution histological images of the H&E-stained sections were recorded using a Pannoramic MIDI digital slide scanner (3D Histech, Budapest, Hungary).

2.5. Immunofluorescence

For the time-course experiments, slide-mounted frozen sections were dried for 3 h before being washed three times in PBS containing 0.2% v/v Triton X-100 (Sigma-Aldrich) (PBS-Tx) for 5 min at room temperature. Sections were then incubated in 10% w/v neutral buffered formalin (Sigma-Aldrich) for 10 min at room temperature, then washed three times in pre-chilled PBS-Tx (4 °C) for 5 min. Antigen retrieval was then performed as described in Section 2.4, followed by three washes for 5 min in PBS-Tx at room temperature prior to the commencement of immunofluorescence. Blocking was performed by incubating sections in 10% v/v Normal Goat Serum solution (Merck-Millipore, VIC, Australia) in PBS-Tx for 1 h at room temperature. Sections were then incubated in a humid chamber overnight at 4 °C with primary antibody, i.e., mouse EM48 anti-huntingtin protein antibody (MAB5374, Merck-Millipore, Kilsyth, Australia) diluted 1/100 in 2% normal goat serum and PBS-Tx and washed three times for 5 min with PBS-Tx at room temperature. To visualize immunoreactivity, sections were washed three times with PBS-Tx, followed by incubation in a humid chamber for 1 h at room temperature with the secondary antibody - Alexa Flour 594 donkey anti-mouse (ab150108; Abcam, VIC, Australia) diluted 1/200 in PBS-Tx. From this step onwards, slide-mounted sections were covered to shield from light. After washing the sections for three times in PBS, the nuclei were counterstained with 4`, 6-diamidino-2-phenylindole (DAPI, Sigma-Aldrich) (0.1 μg/ml) for 5 min at room temperature. Sections were then cover slipped using a fluorescent mounting medium (Dako, Glostrup, Denmark). The slides were dried overnight and then examined using an Olympus BX61 light microscope equipped with a monochrome camera to capture fluorescent images. Digital images were captured as described previously in Section 2.4.

2.6. Multivariate analysis of MALDI-MSI data

The sample preparation, data acquisition, pre-processing, and analysis of MALDI-MSI data were followed as described (Supplementary note 1.1) (Farzana et al., 2022). The data from all age groups were combined into a single analysis file using the MALDI-MSI analysis software SCiLS Lab (SCiLS Lab Version 7.02.10980-2019c Bremen, Germany). This was followed by visual inspection to identify the most frequently detected *m/z* peaks that showed a consistent spatial distribution across all the datasets (absolute peak intensity >50,000).

MSI datasets from healthy wild-type littermate control mice ($n = 6$ 1:1 male: female) were subjected to segmentation using probabilistic latent semantic analysis with deterministic initialization (PLSA-DI) in SCiLS Lab to assess the separability of mouse hippocampal MSI dataset into distinct spatial patterns matching to defined anatomical regions, based on lipid compositions, in an unsupervised manner. The combination of lipids that strongly contribute to the patterns observed in each PLSA-DI component was determined by screening for *m/z* peaks with the highest loading values. The higher the loading value, the higher the contribution of the individual *m/z* peak in discriminating that component from the other components. The top three ranked lipid species were selected as the signature lipids of each PLSA-DI component.

Next, the PLSA-DI component that best matched the spatial expression of hippocampal formation was selected and further segmented using a k-mean clustering algorithm with edge-preserving image. Subsequently, the k-mean clusters were provided as class labels to train a model using Fisher's linear discriminant analysis (LDA), a supervised analysis method with 10-fold cross-validation. The trained classification model (89.6% accuracy) was then used to predict and extract components corresponding to the spatial distribution patterns of our regions of interest (ROI), i.e., CA1 and CA3 and DG hippocampal sub-fields from the age-matched WT and HD replicate datasets. In addition, the lipid signatures of each mouse hippocampal subfields (CA1, CA3 and DG) were identified according to a series of tests as outlined in Supplemental note 2.1.

2.7. Statistical analysis of MALDI-MSI data

Lipid ion abundances within each of the hippocampal subfields (CA1, CA3 and DG) of HD and WT sections were normalized to the signal intensities of an internal standard (sodium anthraquinone-2-sulfonate. The internal standard peak (*m/z* 287.00197) was searched for within a 50 mDa range. Mean abundances of individual lipid features from each hippocampal subfield (CA1, CA3 and DG subfields) of WT and HD mice ($n = 6$/group, 3 males and 3 females) were compared using Receiver Operating Characteristics (ROC) and two-way ANOVA test to screen for gender-genotype interactions. ROC analysis was performed between each WT-HD mice matched replicate pair to identify lipids that most strongly differentiate between WT and HD mice. To account for any differences in area of each hippocampal subfield between WT and HD groups, a matching number of pixels were randomly sampled during ROC analysis using SCiLS Lab. For the second approach, the data matrices containing normalized intensities of the lipid species were exported from SCiLS Lab and subjected to batch-effect correction using Combining Batches of Gene Expression Microarray Data (ComBat) from the Surrogate Variable Analysis (sva) R package (Johnson et al., 2007; Leek, 2014). Subsequently, we applied a logarithmic transformation to the signal intensities for approximation to normal distributions (Feng et al., 2014) and used linear mixed models (two-way ANOVA) (Wanichthanarak et al., 2019), with genotype as fixed effects and batch effects as random effects. Differences were considered statistically significant at area under the curve (AUC) >0.75 and < 0.25, in addition to the criterion of FDR-adjusted *P* value from two-way ANOVA <0.05. All *P* values were adjusted using Benjamini-Hochberg corrections (Benjamini and Hochberg, 1995). To capture subtle differences in lipid abundances that can be highly associative of HD phenotype, we accepted a relaxed threshold for $\log_2$(FC) of −0.5 and 0.5 (corresponding to a 30% change in lipid abundance). Finally, relative quantification and differential analysis of ^{2}H incorporation between WT and HD mice and pathway enrichment analysis was performed using KineticMSI package, an in-house developed R-based software (Farzana et al., 2022).

2.8. LC-MS/MS data analysis

Mouse hippocampal tissues from the matched brain hemispheres (right) were subjected to monophasic lipid extraction method as described previously (Farzana et al., 2022; Lydic et al., 2014). LC-MS/MS data were collected and analyzed using a Vanquish ultra-high-performance liquid chromatography (UHPLC) coupled to an Orbitrap Fusion Lumos MS (Thermo Fisher Scientific) in positive and negative ion mode using the parameters described previously (Farzana et al., 2022; Wang et al., 2020).

Data were processed with MS Dial 4.70 (Tsugawa et al., 2015) using the settings described previously (Farzana et al., 2022; Lau et al., 2022). We confirmed the identity of the parent lipid species from MS-only MSI data by comparing the sum composition of lipids with those identified by LC-MS/MS. For identification and quantification of ganglioside lipids, MS data at negative mode were processed using LipidSearch software v.4.2.23 (Thermo Fisher Scientific) (see Supplementary note 1.3 for details). For samples without ^{2}H labelling, normalization of the LC peak areas of identified lipid ions was performed to the tissue weight and then to the peak areas and quantities of the corresponding internal lipid standards in the same lipid class. The peak areas of each internal standard were extracted based on expected *m/z* value using Skyline 20.2.0. For the lipid classes without correspondent stable isotope-labelled lipid standards, the LC peak areas of identified lipid ions were

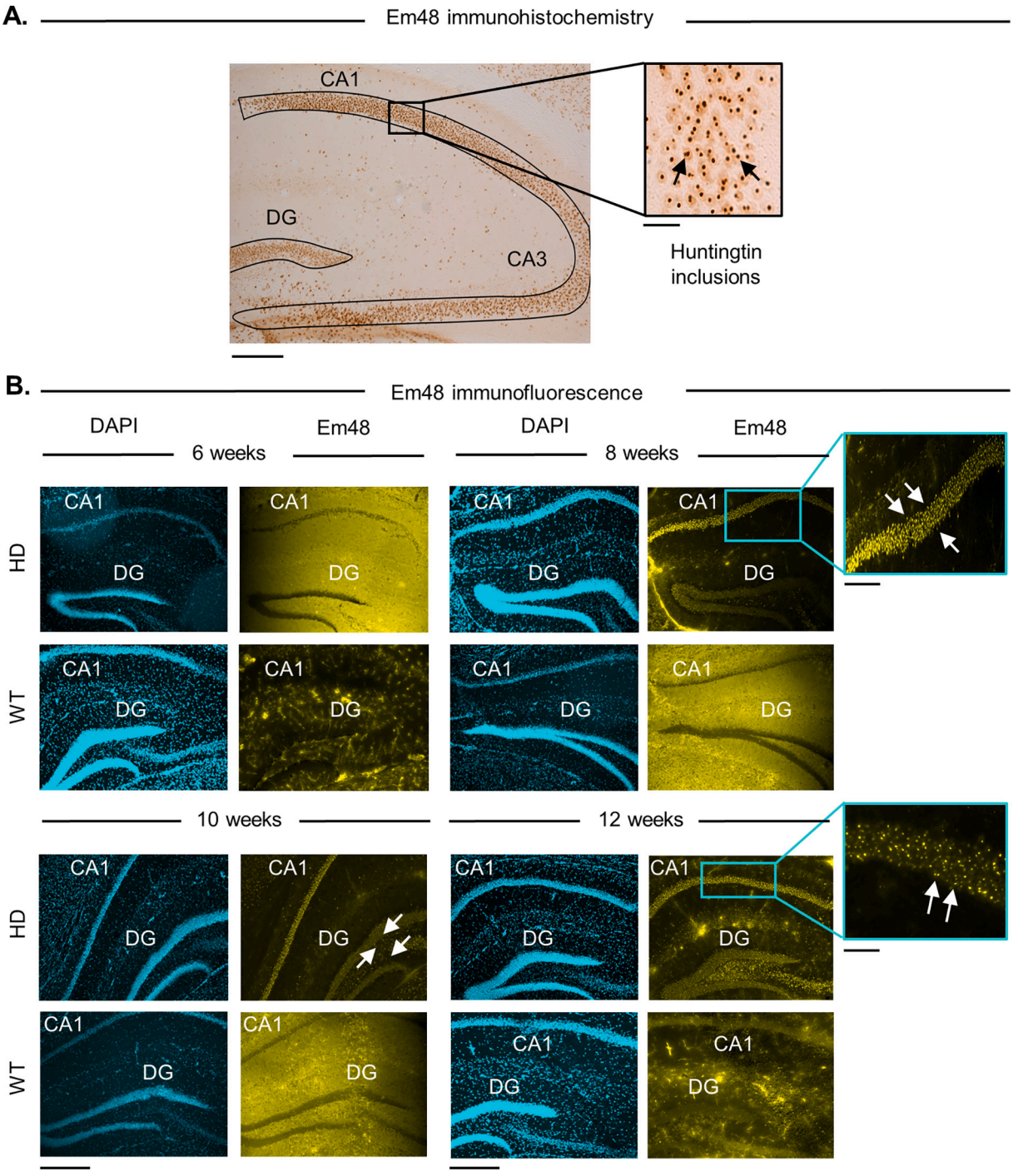

Fig. 1. Time-course analysis to track the appearance of inclusions in the hippocampus of HD mice at 6, 8, 10 and 12 weeks of age. (A) Representative image showing huntingtin inclusions, as detected by Em48 immunohistochemistry in the HD hippocampus of R6/1 mouse model (12 weeks). Black arrows highlight selected inclusions. Hippocampal subfields are labelled in white. These include Cornu Ammonis (CA1) pyramidal cell layer and the dentate gyrus (DG) granule cell layer. (B) Immunofluorescence single-channel micrographs of Em48 (yellow) used for localizing huntingtin inclusions in hippocampal formation of HD mice ($n = 3$/group) and DAPI (cyan) used as a nuclear counterstain. Lack of Em48-labelling (inclusions) at 6-weeks; appearance of inclusions at 8-weeks, shown at a higher magnification to demonstrate Em48-labelling (white arrows) and increase in inclusion density at 10- and 12-weeks. Scale bars, 100 μm; inset, 20 μm. (For interpretation of the references to colour in this figure legend, the reader is referred to the web version of this article.)

normalized as follows: the LPG against the PG (18:1-D7_15:0), the LPA, PA and LPS against the PS (18:1-D7_15:0), the Hex1Cer against the Cer (d18:1-D7/16:0). All results reported here are for relative quantification only (see Supplementary note 1.3 for details).

For samples with ^{2}H labelling, data were pre-processed as described previously (Farzana et al., 2022). Finally, we used two-way analysis of variance (ANOVA) to screen for gender-genotype interactions and performed statistical comparison of steady-state lipid abundances (i.e., pmol/mg tissue) ^{2}H incorporation between WT and HD mice using ANOVA followed by Tukey HSD (Honestly significant difference) post-hoc testing with P value <0.05, using the procedure detailed in the KineticMSI R package (Farzana et al., 2022).

3. Results

3.1. Characterization of inclusion bodies in mouse hippocampal subfields of R6/1 HD mice

First, we used immunohistochemistry to validate the presence of a dense population of neuronal intranuclear inclusions in the mouse hippocampal sub-fields (CA (1–3) and DG) of the HD mice at 12 weeks of age (Fig. 1A) (Rattray et al., 2013; Lazic et al., 2004). Next, we assessed the age at which huntingtin inclusions first formed. Our results showed the presence of neuronal intranuclear inclusions in the mouse hippocampus of the HD mice at 8 weeks of age, but not earlier. The inclusions became progressively more densely distributed at 10 and 12 weeks of age (Fig. 1B). Based on these findings, we hereon defined 6 weeks of age as 'pre-inclusion manifestation' and 12 (Fig. 1B) and 16 weeks of age as 'post-inclusion manifestation' (Fig. S1). By way of reference, 6 weeks of age is prior to the onset of behavioural changes (including depression-like and cognitive deficits) in the mouse model (Naver et al., 2003).

3.2. Spatial mapping of lipids of mouse hippocampus

MALDI-MSI was used to assess spatial metabolite levels in one hemisphere of the mouse brain at different ages and HD versus WT status. The matched brain hemisphere was assessed by LC-MS/MS for a broader coverage of the lipid composition and to confirm the annotation of lipids in MSI data (Fig. S2). MALDI-MSI analysis identified 75.1% glycerophospholipids and 24.9% sphingolipids of the total species level annotated lipids. The lipidome identified covered all major lipid classes: phosphatidylinositol (PI), phosphatidylethanolamine (PE), including plasmalogen PE (PE-E), phosphatidylserine (PS), phosphatidylglycerol (PG), phosphatidic acid (PA), cardiolipins (CL), ceramides (Cer), Hexosylceramides (HexCer), sulfatides (ST) and gangliosides (GM1, GD1a, GA1 and GT3) (Fig. 2A and Table S1). A combined total of 879 lipids were identified by LC-MS/MS analysis at the species (308) and molecular species level (571) (Table S2). Phosphatidylcholine (PC) and sphingomyelin (SM) were identified by LC-MS/MS exclusively (Fig. 2A).

Next, we mapped the spatial distributions of the major brain lipid classes in the mouse hippocampus. While the majority of glycerophospholipids (including PA, PE, PI, PS, PG) and sphingolipids like gangliosides (GM1, GD1a, GA1 and GT3) were widely distributed across neuronal projections (axons and dendrites), sulfatides were

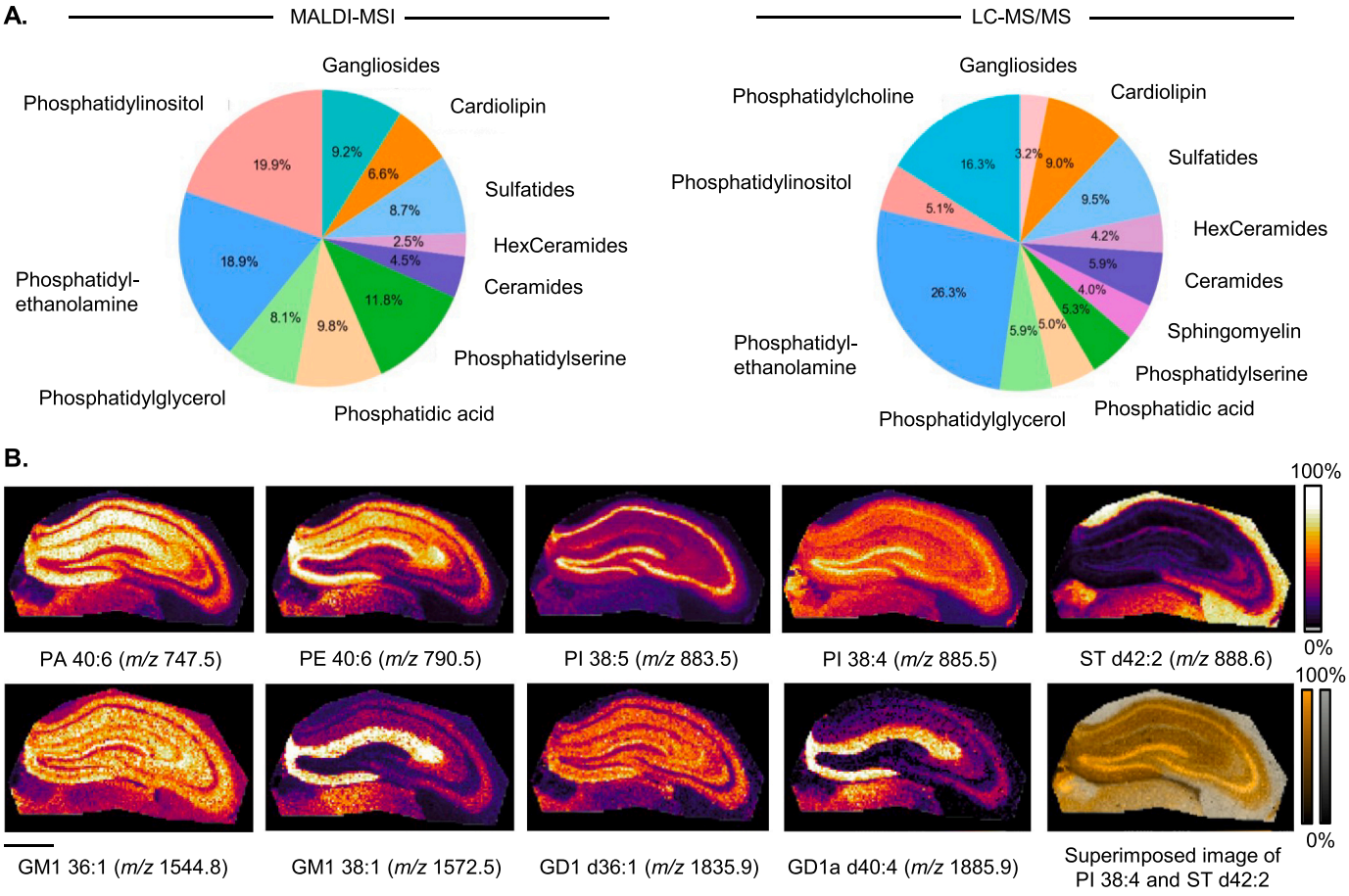

Fig. 2. Overview of lipid classes detected in the mouse hippocampus. Pie chart displaying the different lipid classes detected in WT and HD mouse hippocampus by (A) MALDI-MSI in negative ionization mode. (B) LC-MS/MS in positive & negative ionization mode. (B) Representative spatial distribution of lipid species including PA 40:6, PE 40:6, PI 38:5, PI 38:4, ST d42:2, GM1 36:1, GM1 38:1, GD1 d36:1 and GD1a d40:4 that were identified by MSI in WT mouse hippocampus. The colors in the superimposed image represent the grey matter-specific, PI (38:4) (orange) and white matter-specific ST (d42:2) (grey) (Scale bars, 1 mm).

preferentially localized to the white matter tracks of the mouse hippocampus (Fig. 2B). We also found that structurally similar lipids such as PI (38:5) and PI (38:4), which differ only by a single double bond, displayed stark differences in localization. The C18- and C20-species of GM1 (d36:1 and 38:0) and GD1a (d36:1 and d40:4) also showed distinct patterns (Fig. 2B), similar to a previously reported study (Sugiura et al., 2008).

3.3. Lipidome analysis of mouse hippocampal formation, an inclusion-dense area

The overlaid distribution of the grey matter-specific PI (38:4) (orange) and white matter-specific ST (d42:2) (grey) demonstrated an excellent apparent demarcation of the mouse hippocampus from surrounding tissue by MALDI-MSI (Fig. 2B). We explored whether lipid

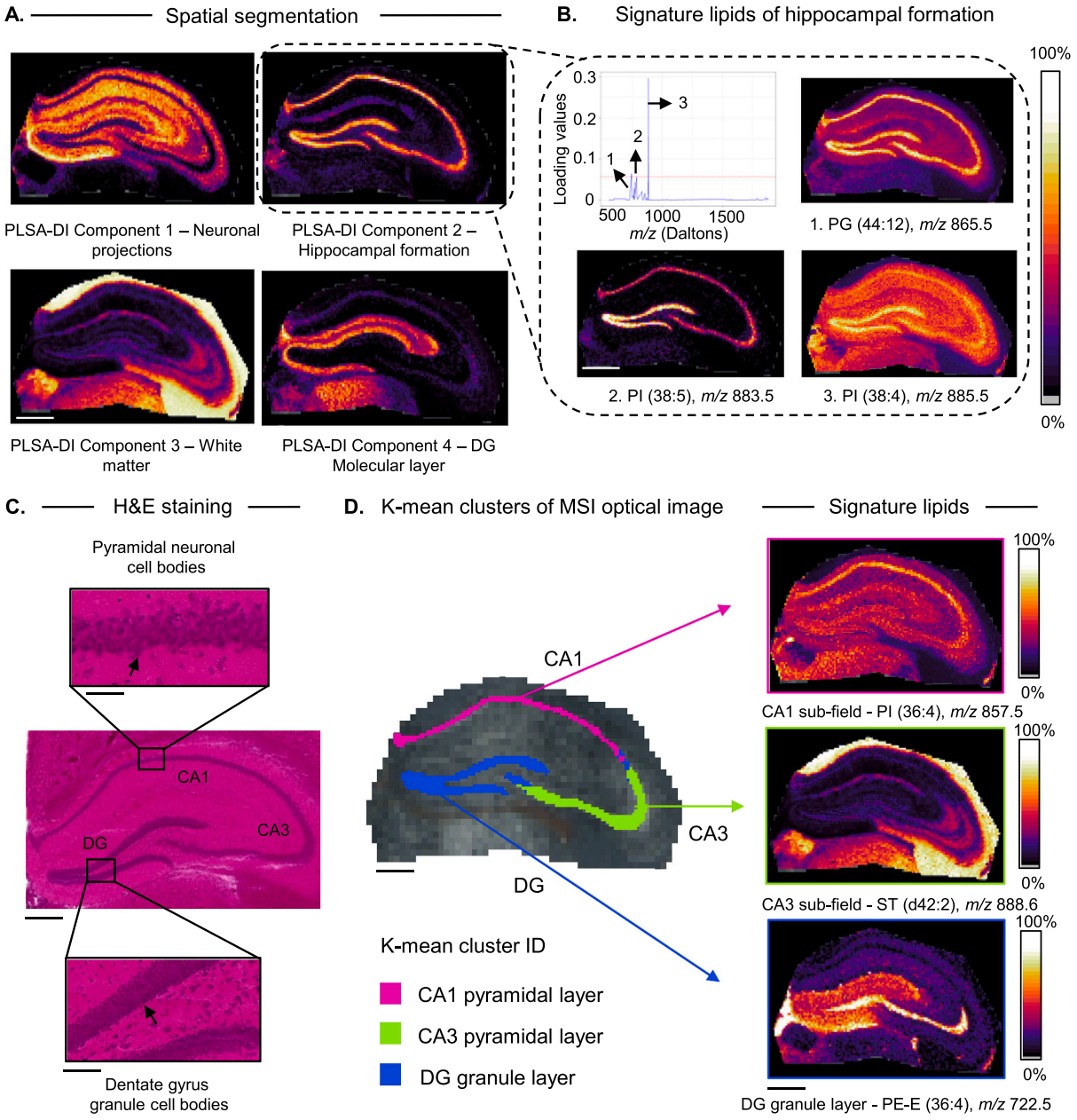

Fig. 3. Strategy used for segmentation of a representative WT mouse hippocampus (16 weeks) MSI dataset, based on lipid compositions. Here, we show the distinct spatial expression patterns, obtained by applying PLSA-DI. We observed similar spatial patterns across all replicates of WT and HD mice at the three age groups examined. (A) PLSA-DI Component 1 – Neuronal projections (axons and dendrites); PLSA-DI Component 2 – Hippocampal formation (pyramidal layer and dentate gyrus granule layer); PLSA-DI Component 3 – White matter and PLSA-DI Component 4 – DG Molecular layer. (B) Identification of signature lipids in the mouse hippocampal formation, an area densely populated by neuronal cell bodies containing huntingtin inclusions. Loading plot of PLSA-DI component and the top three ranked signature lipidomic features of mouse hippocampal formation that include PG 44:12, *m/z* 865.5; PI 38:5, *m/z* 883.5 and PI 38:4, *m/z* 885.5. (Scale bars, 500 μm). (C) H&E-stained image of mouse hippocampus highlighting the differentiation of nuclei (blue) within the neuronal cell bodies of mouse hippocampal pyramidal layers (CA1 and CA3 subfields) and the granule cells of dentate gyrus (DG) from the cytoplasm (pink). Neuronal cell bodies in the hippocampal pyramidal layer (CA1 and CA3 subfields) and the granule cells of dentate gyrus (DG) are shown in the inset (black arrows). (D). Segmentation map of the optical MSI image providing a visual representation of distinct spatial patterns found within the mouse hippocampal formation, based on lipid compositions, obtained by applying k-mean clustering analysis using SCiLS Lab software. The top three k-mean clusters include: CA1, CA3 and DG hippocampal subfields. The CA2 subfield was not observed as an obvious cluster in our study. Signature lipids of CA1 subfield – PI 36:4, *m/z* 857.5; CA3 subfield – STd42:2, *m/z* 888.6 and DG layer – PE-E (36:4), *m/z* 722.5 (Scale bars, 1 mm). (For interpretation of the references to colour in this figure legend, the reader is referred to the web version of this article.)

composition differences for distinct brain regions could define the anatomical boundaries of the brain regions in a non-subjective manner. For this, we applied unsupervised analysis methods and segmented the hippocampus of individual replicates of WT and HD mice (n = 6 1:1 male: female) based on lipid compositions. Using PLSA-DI, we identified four components that closely aligned with the grey matter composed of neuronal projections (axons and dendrites) (PLSA-DI component 1), hippocampal formation (Fig. 3B PLSA-DI component 2), white matter or myelinated tracks (Fig. 3C PLSA-DI component 3), and the molecular layer of the dentate gyrus (Fig. 3D PLSA-DI component 4) depicted in the Allen Mouse Brain Atlas (Dong, 2008). We selected PLSA-DI component 2 as our region of interest as it provided the closest alignment with the hippocampal formation that showed profound inclusion formation. PG (44:12) and PIs including PI (38:4), PI (38:5), PI (36:4), PI (38:6) and PI (40:6) were found to be the major contributors to the PLS-DA component 2 as assessed by their loading values (Fig. 3B). These PI lipids are known to be enriched in neurons (Merrill et al., 2017; Takamori et al., 2006; Tian et al., 2019), and hence provided us with a hippocampal neuron lipid set for further analysis. PG (44:12), a docosahexaenoic acid (DHA)-containing lipid species, has not been previously linked clearly to the neuronal cell bodies of mouse hippocampus, but the close alignment with the other lipids known to, suggests it is enriched in hippocampal neuronal soma (Fig. 3B).

Since the mouse hippocampus is composed of functionally distinct subfields as observed in the H&E-stained hippocampal section (Fig. 3C), we expected metabolite levels to differ between the subfields. To further segment these regions, we applied a k-means clustering approach based on lipid compositions. The resulting segmentation map and the top three k-mean clusters showed a close alignment with the anatomical structures within the hippocampus formation corresponding to the CA1 and CA3 pyramidal cell layer and DG granule cell layer depicted in the Allen Mouse Brain Atlas (Dong, 2008) (Fig. 3D). We also characterized the lipidome of these hippocampal subfields (CA1, CA3 and DG) in wild-type control mice and identified the signature lipids of each subfield (Fig. 3D, Fig. S3, S4 and Supplementary note 2.1). These hippocampal subfields displayed a lipid signature that closely aligned with the known functions of each subfield (for a detailed explanation, see supplementary note 2.2).

3.4. *Selective loss of neuronal signature lipids in hippocampal subfields in HD mice*

Next, we measured the changes in relative abundances of neuronal membrane lipids in areas dense in inclusions within the hippocampal subfields (CA1, CA3 and DG) at different ages and HD versus WT status. Animals of both sexes were pooled together to examine HD-specific effects, as we found no significant sex-genotype effects using two-way ANOVA (Table S4). We created a custom-curated pathway database (Table S3) by categorizing the detected lipids into neuronal cell body, axonal, synaptic, myelin (oligodendrocyte), mitochondrial and astrocyte enriched lipids, based on previously published cell type-specific lipidome of the mammalian brain (Merrill et al., 2017; Takamori et al., 2006; Tian et al., 2019; van Echten-Deckert and Herget, 2006; Fitzner et al., 2020; Kaya et al., 2017; Chen et al., 2018a; Neumann et al., 2019; Xie et al., 2020).

A total of 5, 48 and 59 annotated lipid species showed differential abundances in the hippocampal subfield of 6-, 12- and 16-week-old HD mice respectively (Table S4). MALDI-MSI ion images for lipid features that showed differential abundance in hippocampal subfields (CA1, CA3 and DG) of HD mice, relative to WT control mice at three age groups (6, 12 and 16 weeks) are shown in Fig. S5. In the CA1 subfield, there were no significant differences in lipid abundances in the 6-week-old group between WT and HD mice (Fig. 4A). However, at 12 weeks of age, significant differences were revealed, with HD mice showing a lower abundance of axonal lipids (P = 0.01), and lipids in the PS class (P = 0.001), including PS (40:6), PS (40:7), PS (44:12), PS (46:8), PS (48:9), PS (48:8). Neuronal cell body-enriched lipids were also decreased at 12 weeks, i.e., PI (36:4) and PG (44:12) as well as mitochondria-enriched lipids including PE (38:6), PE (40:7), PE (40:6) and PE (40:5) (Fig. 4A and Table S4). The significantly enriched functional categories associated with these lipids mapped to axonal regeneration (P = 0.002) and activation of brain-derived neurotrophic factor (BDNF) signaling (P = 0.001) (Fig. 4A). These functional categories relate to mechanisms that have been previously implicated in HD pathology (Zuccato et al., 2005; Li and Conforti, 2013). At 16 weeks, we found a gradual increase in the number of lipids showing reduced abundances (n = 21) in the CA1 subfield of HD mice displaying inclusions. Of note, a stark reduction was observed in neuronal cell-body enriched lipids (P = 0.01) such as PI (38:5), PI (36:4), PI (38:6), PI (40:6) and PG (44:12); axonal lipids namely PS (44:12) and PS (40:6); mitochondrial-enriched PE lipid class including PE (34:0), PE (34:1), PE (36:4) and myelin-enriched lipids such as PE-E (50:11) and SHexCer (40:2). (Fig. 4A). Additionally, we observed reductions in synaptic lipids, including phosphatidic acid (PA (32:0), PA (36:4)) and gangliosides (GM1(36:1)), suggesting a change in the lipid composition of neuronal cell bodies and a potential loss of neuronal architecture at this age.

Of note were changes in lipid abundances in the CA3 hippocampal subfield of HD mice at 6 weeks of age, which is prior to both the formation of inclusions and when behavioural and cognitive deficits arise. These lipids include PG (38:3), PG (40:4), PIP (35:1), PE-E (46:9) and PS (46:7) (Fig. 4B). These lipids did not map onto functional pathways of our custom-curated pathway database (Table S3; Fig. 4B). By the time inclusions had formed (12 weeks of age), there was a striking reduction in myelin-enriched lipids, that are signature lipids of this layer (see supplementary note 2.1 and Fig. S3C). These include sulfatides (SHexCer (40:2)), PE-plasmalogens (PE-E (38:6) and PE-E (46:9)) and PI-Ceramides (PI-Cer (40:1)) (Fig. 4B and Table S4). Considering the importance of these lipids in myelin formation and oxidative-stress protection, the observed changes in these lipids may relate to white matter abnormalities and oxidative stress in HD (Palavicini et al., 2016; Jin et al., 2015; Gil-Mohapel et al., 2014; Kuczynski and Reo, 2006). Similar to what was observed in the CA1 subfield, there was a decline in several axonal lipids in the CA3 subfield (P = 0.007), in particular, the phosphatidylserine lipid class (P = 0.0001). These lipids include PS (40:6), PS (36:2), PS (38:4), PS (40:7), PS (40:4), PS (46:8), PS (46:6), PS (48:9), PS (48:8) and PS (36:4). In addition, a significant reduction was observed in mitochondrial-enriched phosphatidylethanolamine (P = 0.005) lipids such as PE (34:1), PE (36:2), PE (36:4), PE (38:4), PE (38:6), PE (40:4), PE (40:5), PE (40:6) and PE (40:7) (Fig. 4B). These changes mapped to functional pathways of axonal regeneration (P = 0.001), activation of BDNF signaling (P = 0.001), hippocampal neurogenesis (P = 0.003), membrane fluidity and dynamics (P = 0.004) and ER-stress protection (P = 0.03) (Fig. 4B). Mechanisms connected to these pathways have been implicated in HD pathology (Zuccato et al., 2005; Li and Conforti, 2013; Li et al., 2001; Sameni et al., 2018; Lee et al., 2012).

At 16 weeks of age, an additional 21 lipids showed a significant reduction in abundance across the CA3 subfield (Fig. 4B). This included synaptic associated phosphatidic acid lipids (PA (32:0), PA (34:1), PA (36:2), PA (36:4), PA (38:5)) and gangliosides (GM1 (36:1)). Further reductions were also observed in the abundances of mitochondria-enriched phosphatidylethanolamine lipids (PE (34:0), PE (36:1), PE (38:5)) and cardiolipins (CL (74:10). Considering that the PE and cardiolipins together are involved in mitochondrial bioenergetics and function, ATP synthesis, and hippocampal-dependent cognitive functions (Cole et al., 2018; Aufschnaiter et al., 2017), these changes may have implications for mitochondrial (Kim et al., 2010) and cognitive dysfunction previously reported in HD (Paulsen, 2011). Lipids that increased in abundance at 16 weeks mapped to pathways protecting against neuronal excitotoxicity via regulation of glutamate *N*-methyl-D-aspartate (NMDA) receptors (P = 0.03) (Fig. 4B).

Relatively fewer changes in lipid abundances were detected in the

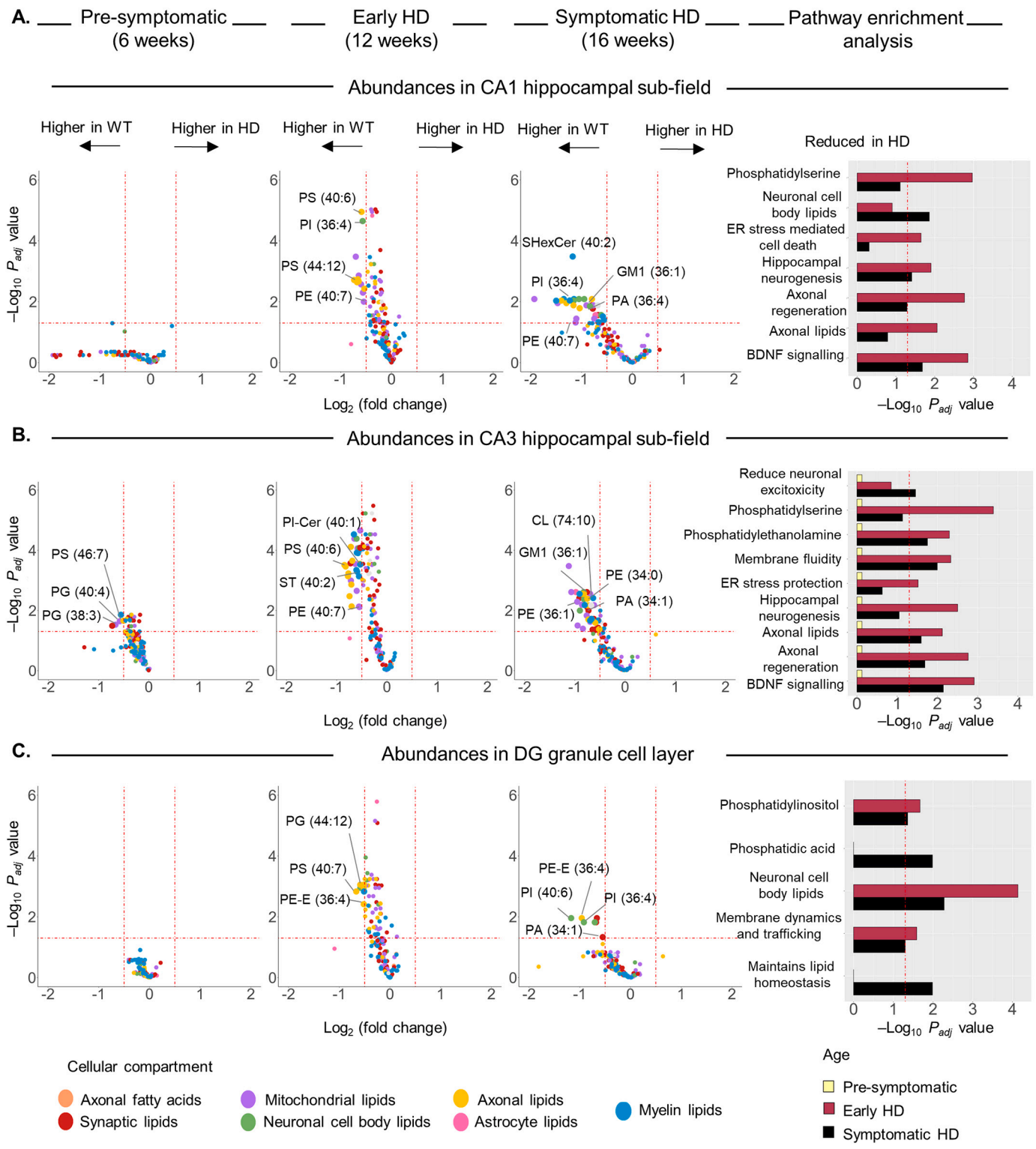

Fig. 4. Differential analysis of relative abundances of lipids in hippocampal subfields (CA1, CA3 and DG) of WT and HD mice ($n = 6$/group) at three age groups (6, 12 and 16 weeks). Volcano plots showing comparison of normalized lipid abundances between WT and HD mice in (A) CA1 hippocampal subfield; (B) CA3 hippocampal subfield and (C) DG granule cell layer. Group bar plot representation showing significantly enriched functional categories revealed by pathway enrichment analysis (Fisher exact test), using an in-house custom-curated pathway database (Table S3). Selected significantly enriched functional categories are coloured by age group in (A) CA1 hippocampal subfield; (B) CA3 hippocampal subfield and (C) DG granule cell layer. Red line denotes significance $P < 0.05$. (For interpretation of the references to colour in this figure legend, the reader is referred to the web version of this article.)

dentate gyrus region compared to the CA1 and CA3-subfields of the HD mice. There were no differences in lipid abundances between WT and HD mice at 6 weeks of age (Fig. 4C). However, at 12 weeks there was a striking loss of neuronal cell body-enriched lipids ($P = 0.0005$) belonging to the PI lipid class ($P = 0.01$), including PI (36:4), PI (38:6), PI (38:5) and PI (40:6) (Fig. 4C). The pathway enrichment analysis revealed membrane trafficking and dynamics as the significantly impacted functional category ($P = 0.01$) associated with reductions observed in the PI lipid class (Fig. 4C). Additionally, we found a significant reduction in PS lipid class, including PS (40:7), PS (40:6), PS (46:6), PS (46:7), PS (46:8) and PS (48:9) in the DG subfield at 12 weeks (Fig. 4C). At 16 weeks, we found a further reduction of the phosphatic acid lipid class ($P = 0.01$) including PA (36:4), PA (32:0) and PA (34:1) in HD mice, potentially contributing to lipid dyshomeostasis (Tanguy et al., 2019) (P = 0.01) (Fig. 4C) at this timepoint.

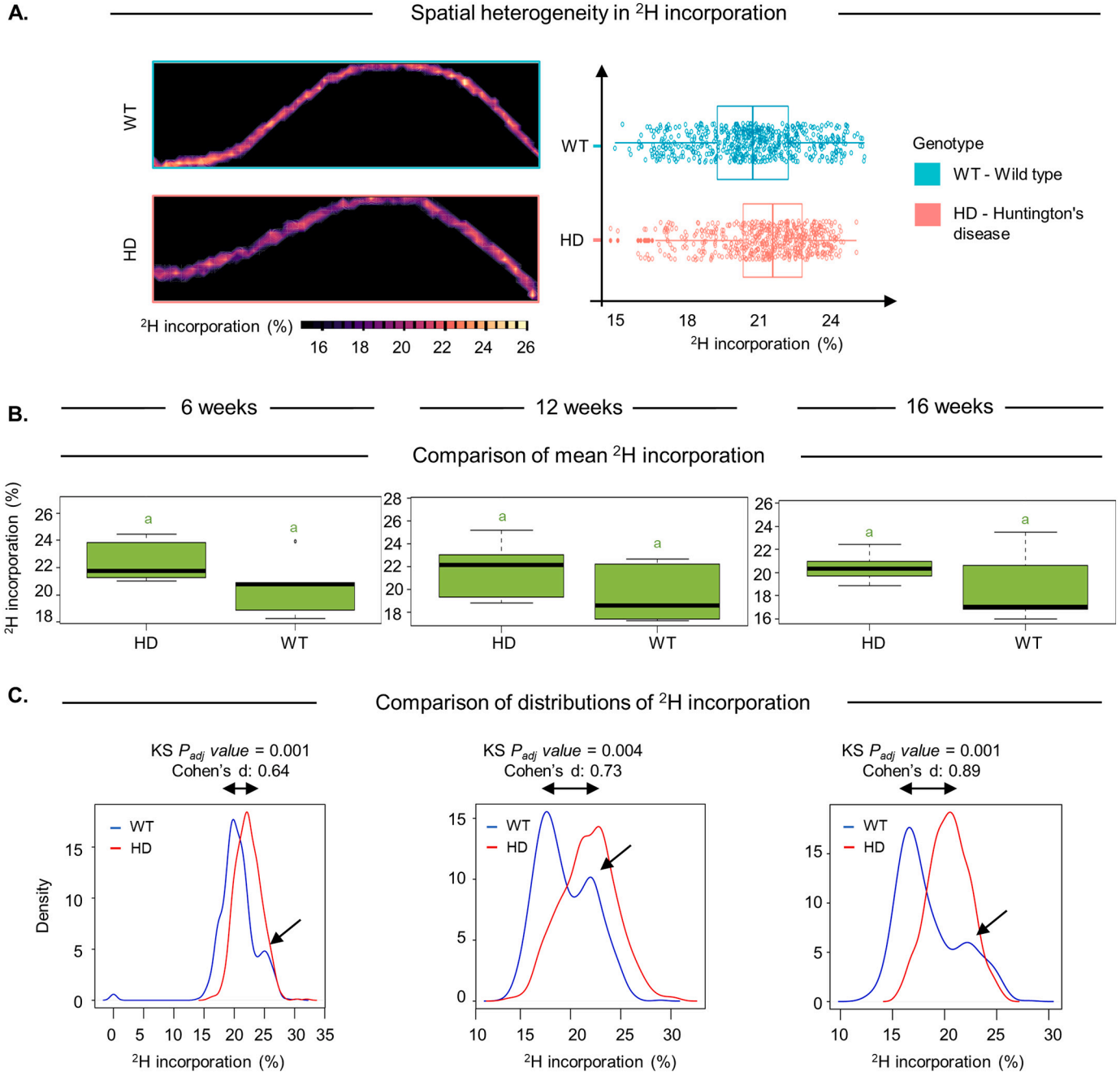

Fig. 5. Differential analysis of ^{2}H incorporation between WT and HD mice using CA1 hippocampal subfield and the neuronal lipid, PI (36:4) as an example. (A). Visualization of KineticMSI images displaying spatial heterogeneity in ^{2}H incorporation in PI (36:4) of a representative WT and HD replicate dataset (16 weeks). The colour gradations across the pixels represent the varying degree of ^{2}H incorporation within the CA1 subfield of WT and HD mice, showing zones of higher (gold) and lower (dark purple) ^{2}H incorporation. Boxplot representation showing the distributions of ^{2}H incorporation in PI (36:4) in CA1 subfield of replicate datasets from WT and HD mice ($n = 6$/group). (B) Comparison of mean ^{2}H incorporation in PI (36:4) across CA1 subfield using two-way ANOVA (6, 12 and 16 weeks). (C) Comparison of shapes and overlap of distributions of ^{2}H incorporation using Kolmogorov-Smirnov test and effect size estimation (Cohen's d values). The black arrows show the change from a bimodal distribution in WT to a unimodal distribution in HD mice. (For interpretation of the references to colour in this figure legend, the reader is referred to the web version of this article.)

3.5. Lipid synthesis is altered prior to inclusions forming

For further insight into the details of the metabolic changes, we performed stable isotope (^{2}H) incorporation experiments to measure lipid synthesis. Healthy control mice were labelled with ^2H_2O for up to 64 days and culled at different time points corresponding to 2-, 4-, 8-, 16-, 32- and 64-days after the start of labelling to obtain estimated half-times of lipid turnovers (T_{50}). An eight-day timepoint was chosen as the optimum timeframe for labelling mice on the basis that ~30–50% ^{2}H was incorporated into the metabolic targets (T_{50}), which was assessed by at least a single substitution of ^{1}H atom by ^{2}H (for a detailed procedure, see Supplementary Note 2.3 and Fig. S6). Similar labelling percentages of ^{2}H were observed at eight-day timepoint across major lipid classes examined in our study including PC, PE, PI, PS, PG, CL, Cer, HexCer, ST and Cer.

First, we examined ^{2}H incorporation in the neuronal lipid PI (36:4), *m/z* 857.5, because it was a signature lipid of the CA1 hippocampal subfield and was shown to be reduced in the HD mice compared to the WT mice by 12 weeks of age. PI (36:4) also showed an altered ^{2}H incorporation in HD mice compared to WT controls in all of the mouse ages assessed (Fig. 5). Comparison of mean ^{2}H incorporation in PI (36:4) across the CA1 subfield showed no significant differences in apparent ^{2}H incorporation between WT and HD mice at 6, 12 and 16 weeks timepoints (Fig. 5B). Closer examination indicated intra-tissue spatial heterogeneity in ^{2}H incorporation in PI (36:4) within each hippocampal subfield of WT and HD mice. This pixel-to-pixel variability in ^{2}H incorporation in PI (36:4) was evidenced by a range in ^{2}H incorporation (16–26%) in the MSI pixels and a non-uniform speckled appearance of ^{2}H labelling in the reconstructed kMSI images of the CA1 hippocampal subfields of WT and HD mice. (Fig. 5A). Indeed, a comparison of the distributions of ^{2}H incorporation in MSI pixels between WT and HD mice revealed a significant difference in the CA1 subfield of HD mice before inclusions formed (6 weeks) (Kolmogorov-Smirnov test, FDR-adjusted *P* value = 0.001 and Cohen's d value = 0.64) and after inclusions formed (12 and 16 weeks) (Kolmogorov-Smirnov test, FDR-adjusted *P* value = 0.004 and 0.001; Cohen's d value = 0.73 and 0.89 respectively). A significant increase in ^{2}H incorporation in PI (36:4) was observed in HD mice, as evident by the rightward shift in the distributions of ^{2}H incorporation in HD mice (Fig. 5C). Additionally, the shift in a bimodal distribution of ^{2}H incorporation observed in WT (shown by the black arrows in Fig. 5C) to a unimodal distribution in HD suggested the presence of distinct ^{2}H incorporation subsets within the hippocampal subfields of WT and HD, thus confirming intra-tissue spatial variation in ^{2}H incorporation.

Comparison of distributions of ^{2}H incorporation across all the lipid features between WT and HD mice showed an increased ^{2}H incorporation in a vast majority of neuronal lipids consistently in all the three HD age groups examined (6, 12 and 16 weeks) across the CA1 (Fig. 6A), CA3 (Fig. 6B) and DG granule cell layer (Fig. 6C). To determine whether the measures can be explained by changes in lipid synthesis rates, we compared the relative abundances of ^{2}H labelled synthesized lipid pools between WT and HD mice. The results support the conclusion of elevated lipid synthesis in HD mice both before (6 weeks) and after the appearance of inclusions, and for the effect to arise in all the examined subfields of the hippocampal formation (Fig. S7).

Of the lipids that were significantly increased in ^{2}H incorporation in HD mice, neuronal cell body lipids belonging to the PI lipid class such as PI (36:4) and PI (38:5), were the most significantly changed (Fig. 6A, B and C). These lipids mapped to the functional pathway of membrane trafficking and dynamics (Di Paolo and De Camilli, 2006; Li et al., 2020). A handful of lipids that showed a significant reduction in synthesis in HD mice include PG (44:5) in the CA3 subfield at 6 weeks; and PS (46:8) and PIP (44:3) in the DG layer at 6 and 12 weeks of age, respectively. The decrease in ^{2}H incorporation in mitochondrial-associated PG lipid class aligns with the reduction observed in the abundance of this lipid class in the CA3 subfield of 6 weeks HD mice. As PS can be transported to mitochondria and converted to PE (Tracey et al., 2018), the decrease in ^{2}H incorporation in PS (46:8) may be explained by the conversion of PS to PE, a mitochondrial lipid class that showed increased ^{2}H incorporation in the DG of 6 weeks HD mice. Likewise, the decrease in ^{2}H incorporation in PIP (44:3) may be due to the conversion of PIP to lipid intermediates in the phosphatidylinositol cycle, including PA, PE and PI (Epand, 2017) that showed increased ^{2}H incorporation in 6 weeks HD mice.

3.6. Assessment of the metabolic changes in whole hippocampus by LC-MS/MS

Next, we turned to LC-MS/MS of the matched brain hemispheres to increase lipid coverage and provide a whole tissue analysis of hippocampus (Table S5). Consistent with the MALDI-MSI findings, there were no significant sex-genotype effects (Table S5). At the 6 weeks timepoint, LC-MS/MS revealed a significant reduction in PC lipid class, including PC (32:1), PC (32:2), PC (34:2), PC (36:5) and PC (40:6) in HD mice. PC is the most abundant lipid (58%) among membrane phospholipids (Paoletti et al., 2011) and so disturbances in membrane composition of this lipid class may result in a loss of membrane stability and function. Moreover, PC also serves as a precursor of neurotransmitter acetylcholine (Blusztajn et al., 1987) and plays important roles in the activation of BDNF signaling, synaptogenesis (Che et al., 2018), neuronal differentiation (Paoletti et al., 2011) and neurogenesis (Magaquian et al., 2021), mechanisms that are implicated in HD pathology (Tyebji and Hannan, 2017; Ransome and Hannan, 2013). (Fig. 7A). Lysoglycerophospholipids belonging to PC, PE, PS, PG and PI lipid classes, showed an increase in relative abundances of ($P < 0.0001$) 6-week-old HD mice compared to WT mice. At 12 weeks, lysoglycerophospholipids in PC, PE, PS and PA classes were increased ($P < 0.0001$). These lipids mapped onto the functional pathway of signal transduction (6 weeks; $P = 0.0009$ and 12 weeks; $P = 0.0003$) (Fig. 7A). In contrast to the reductions observed in lipid abundances in the hippocampal subfields (CA1, CA3 and DG) of 12-week-old HD mice by MALDI-MSI, LC-MS/MS analysis of the whole hippocampal showed no significantly reduced lipid abundances (Fig. 7A). This difference reflects the loss of spatially encoded subfield specific metabolic changes when using LC-MS/MS analysis.

LC-MS/MS analysis also showed an increase in the relative abundance of the myelin-enriched sulfatides, such as SHexCer (42:0) ($P = 0.02$) in 6-week-old HD mice and SHexCer (38:0) ($P = 0.02$) and SHexCer (44:6) ($P = 0.03$) in 12-week-old HD mice, compared to WT controls. Indeed the 16-week-old HD mice showed a more pronounced increase in the myelin-enriched lipids ($P = 0.03$), including SM (36:2) and the sulfatide lipid class ($P < 0.0001$). The significantly enriched functional categories associated with these changes were found to be myelin stability ($P = 0.02$) and maintenance of axon-glial interactions ($P = 0.0004$) (Fig. 7A). Sulfatide accumulation has been previously associated with axonal degeneration (Eckhardt et al., 2007) and astrogliosis (Molander-Melin et al., 2004), mechanisms previously implicated in HD pathology (Mazurová et al., 2014; Yang et al., 2020). Consistent with the changes reported by MALDI-MSI at the 16 weeks timepoint, LC-MS/MS analysis also showed a decline in mitochondrial enriched lipids such as PE (33:0) ($P = 0.01$), PE (34:4) ($P = 0.02$), PE (40:6) ($P = 0.04$), CL (64:0) ($P = 0.04$) and CL (73:6) ($P = 0.02$) and synaptic lipids such as PI (32:0) ($P = 0.01$) in HD hippocampi. The significantly enriched category associated with the above changes was neurotransmitter release ($P = 0.02$) (Fig. 7A).

The analysis of the ^{2}H incorporation yielded findings consistent with the MALDI-MSI imaging. Notably, ^{2}H incorporation was increased in the lipids of HD mice as early as 6 weeks of age (Fig. 7B). Key lipids included those in the neuronal cell body (PI (40:6) ($P = 0.04$), PC (34:0) ($P = 0.04$) and PC (34:1) ($P = 0.02$)), synapse (GM1 (d34:1) ($P = 0.004$), GM2 (d36:2) ($P = 0.01$), Cer (42:12) ($P = 0.02$) and PA (38:3) ($P = 0.03$)) and axons (PC (44:12) ($P = 0.002$), PC (36:1) ($P = 0.03$) and PC (36:4) ($P =$

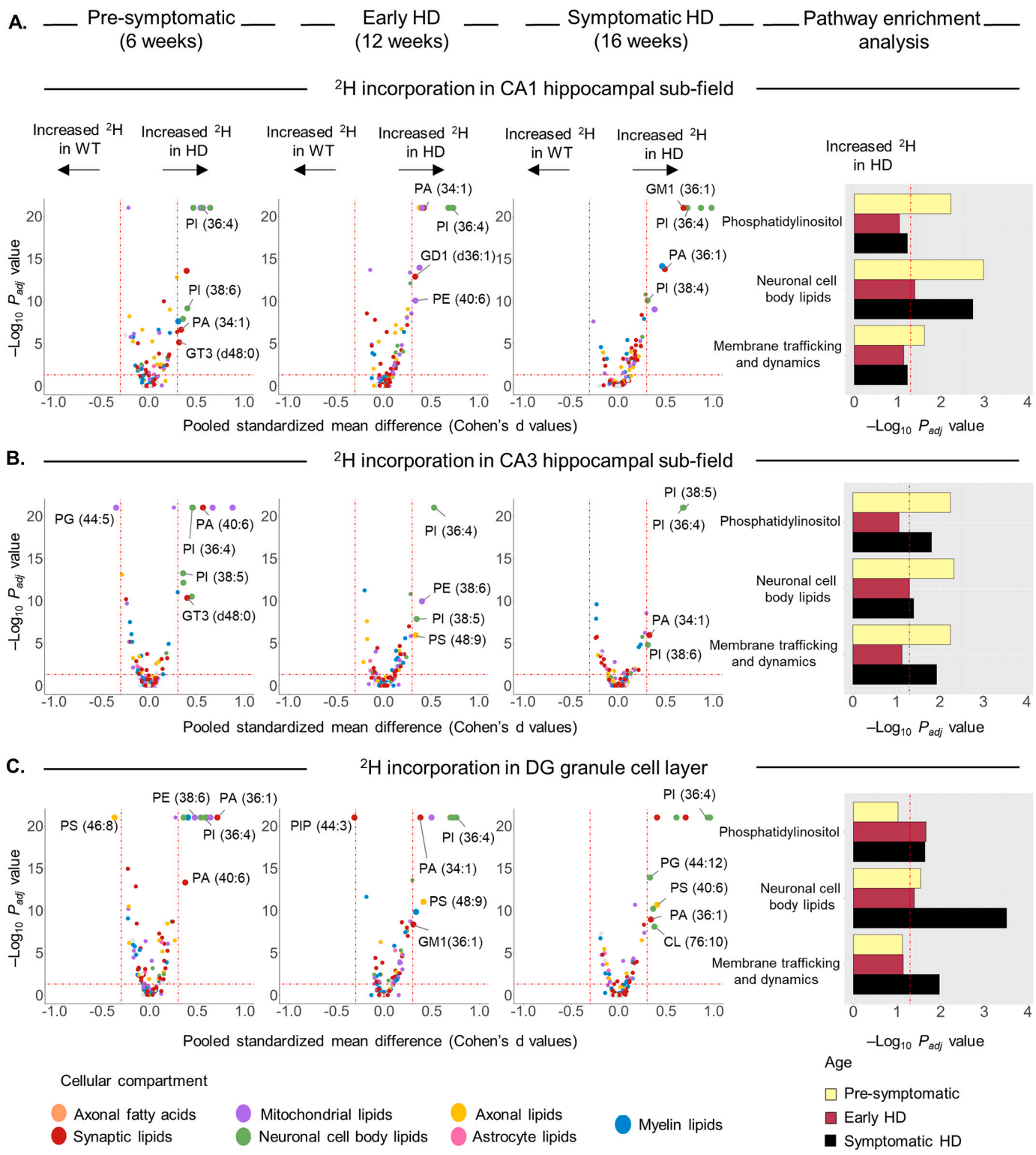

Fig. 6. Differential analysis of ^{2}H incorporation in lipids of hippocampal subfields (CA1, CA3 and DG) of WT and HD mice ($n = 6$/group) at three age groups (6, 12 and 16 weeks) by MALDI-MSI. Volcano plots showing significant changes in ^{2}H incorporation in lipid features of HD mice, relative to WT controls in (A) CA1 hippocampal subfield; (B) CA3 hippocampal subfield and (C) DG granule cell layer. Cohen's d values indicate the standardized difference between two means (difference between two means divided by the pooled standard deviation). Group bar plot representation showing the significantly enriched functional categories revealed by pathway enrichment analysis (Fisher exact test), using an in-house custom-curated pathway database (Table S3). Selected significantly enriched functional categories are coloured by age group in (A) CA1 hippocampal subfield; (B) CA3 hippocampal subfield and (C) DG granule cell layer. Red line denotes significance $P < 0.05$. (For interpretation of the references to colour in this figure legend, the reader is referred to the web version of this article.)

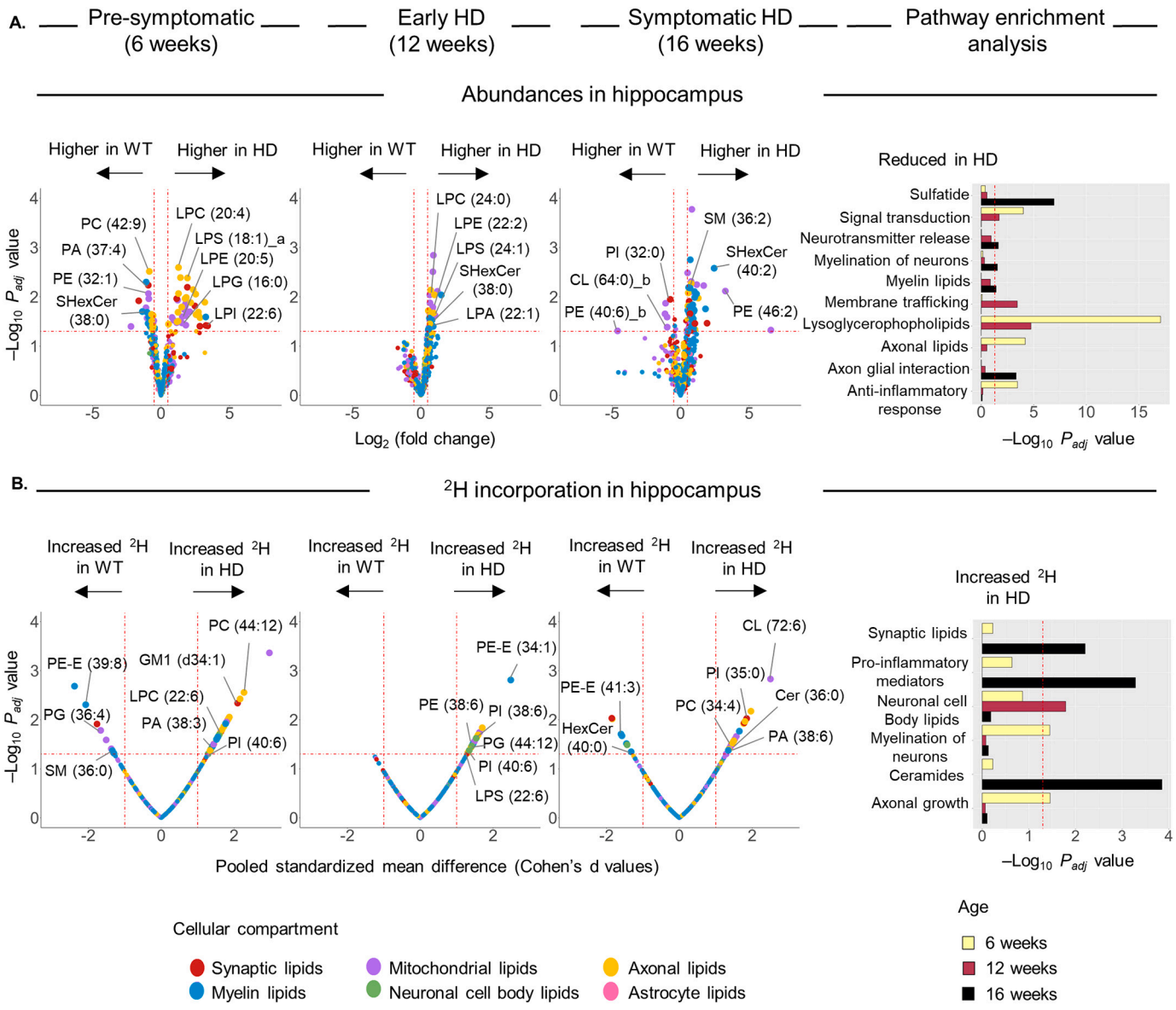

Fig. 7. Differential analysis of relative abundances and ^{2}H incorporation in lipids in hippocampal region of WT and HD mice ($n = 6$/group) at three age groups (6, 12 and 16 weeks) by LC-MS/MS. (A) Volcano plots showing the comparison of lipid abundances between WT and HD mice hippocampi. (B) Volcano plots showing the comparison of ^{2}H incorporation in lipids between WT and HD mice hippocampi. Group bar plot representation showing the significantly enriched functional categories revealed by pathway enrichment analysis (Fisher exact test), using an in-house custom-curated pathway database (Table S3). Selected significantly enriched functional categories are coloured by age group in (A) non-labelled WT and HD mice and (B) ^{2}H labelled WT and HD mice. Red line denotes significance $P < 0.05$. (For interpretation of the references to colour in this figure legend, the reader is referred to the web version of this article.)

0.03)). These lipids mapped onto the axonal growth functional term ($P = 0.03$) (Fig. 7B). Conversely, myelin-specific lipids (SM (36:0) ($P = 0.04$), ether PC (PC-E (39:5)) ($P = 0.04$), ether PE (PE-E (39:8)) ($P = 0.004$) and lipids of the mitochondria (CL (74:10) ($P = 0.03$), CL (74:12) ($P = 0.02$) and PG (36:4) ($P = 0.01$)) showed reduced ^{2}H incorporation in the 6-week-old HD mice. These lipids map onto the neuronal myelination functional term ($P = 0.03$) and may contribute to early white matter abnormalities (myelin loss) and mitochondrial defects reported in HD (Jin et al., 2015; Panov et al., 2002).

The changes observed at the later timepoints (12 and 16 weeks of age) were consistent with MALDI-MSI. Key functional pathways mapped by these changes include neuronal cell body lipids ($P = 0.01$)) and synaptic lipids ($P = 0.006$) in the 12- and 16-week-old HD mice, respectively (Fig. 7B). Additionally, LC-MS/MS analysis also showed increased ^{2}H incorporation in the ceramide lipid class ($P = 0.0001$) that mapped onto the pro-inflammatory response functional term ($P = 0.0005$) in 16-week-old HD mice. Other changes that were not detected by MALDI-MSI included a significant reduction in ^{2}H incorporation in myelin-associated lipid including HexCer (43:1) ($P = 0.03$), HexCer (40:0) ($P = 0.04$), and ether PE (PE-E (32:2) and PE-E (41:3)) ($P = 0.02$ and $P = 0.01$) in 16-week-old HD mice. Myelin-associated lipids are primarily synthesized in oligodendrocytes (Fitzner et al., 2020). Hence, these changes may not have been detected by MALDI-MSI, which focused on the hippocampal subfields that are predominantly rich in neurons, where neuronal density is known to be approximately two-fold higher than non-neuronal cell types (Keller et al., 2018).

4. Discussion

Here we assessed changes in the relative abundances and apparent synthesis rates of neuronal membrane lipids in the hippocampal subfields (CA1, CA3 and DG) of HD mice, areas that are especially dense in

inclusions. The reduced abundance of lipid species in the hippocampus of HD mice measured here is largely in agreement with previous studies assessing lipid changes in different brain regions from symptomatic human HD tissue or animal models, including PA (Hunter et al., 2021; Vodicka et al., 2015), PI (Hunter et al., 2018), PS (Hunter et al., 2021; Mehrotra et al., 2015), PE (Mehrotra et al., 2015), CL (Mehrotra et al., 2015; Iuliano et al., 2021), sulfatides (Hunter et al., 2018) and Ganglioside (GM1) (Hunter et al., 2021; Denny et al., 2010; Maglione et al., 2010; Desplats et al., 2007). Our findings extend this knowledgebase by unmasking changes in lipid abundances and synthesis rates within specific neuronal layers of the hippocampal formation (CA1, CA3 and DG subfields) that are densely populated by inclusions and by finding changes that arise before the appearance of inclusions or onset of a HD-like behavioural and cognitive phenotype in a preclinical model of HD. Our study further defined progressive lipid changes in HD hippocampi that closely correlate with cognitive changes in early and symptomatic stages of HD (Gaura et al., 2017; Colgan et al., 2007), thus pointing to these lipid disturbances potentially contributing to pathological mechanisms underlying hippocampal-dependent cognitive and neuronal dysfunction in HD mice in an age-dependant manner.

Our results appeared to show that there wasn't a large decrease in lipid synthesis rates in a manner that might be expected for a broad-scale quiescence. Instead, the data showed a decrease in key neuronal lipids across the three hippocampal subfields (CA1, CA3 and DG) in HD mice relative to WT controls, but with many of these lipids appearing to also synthesize at higher rates in HD mice. Of note, this increase in lipid synthesis was observed as early as the pre-symptomatic age of HD (6 weeks). This led us to speculate that the overproduction of lipids may serve as a coping or compensatory mechanism to counteract the loss of neuronal lipids and thus represent an adaptive stress response in the early stages of HD. Further supportive evidence of compensatory mechanisms in HD comes from a study by Gaura et al. (2017) (Gaura et al., 2017) demonstrating variability in rates of metabolism in brain regions of HD patients, with hypermetabolism in the cerebellum serving as a compensatory mechanism to cope with the slow striatal metabolism in preclinical gene carriers of HD.

Although a detailed investigation is required to understand the mechanisms underlying increased lipid synthesis in HD, our data points to a role related to endoplasmic reticulum (ER) stress as a driver of lipogenesis (Colgan et al., 2007; Kim et al., 2018). The ER, which is the primary site of lipid synthesis, plays a crucial role in maintaining intracellular lipid homeostasis (Jacquemyn et al., 2017). Enhanced lipid synthesis has been linked with the adaptive cellular response to cope with ER stress (Romero et al., 2018). Recent findings have shown that perturbations in membrane lipid compositions trigger membrane lipid bilayer stress and signal ER stress, activating the adaptive stress response, i.e., the unfolded protein response (UPR) (Ho et al., 2018; Halbleib et al., 2017; Shyu et al., 2019; Torkzaban et al., 2020; Xu and Taubert, 2021). Lipids that were increased in synthesis in the pre-symptomatic mice (6 weeks) included many involved in the ER stress responses, including the neuronal-cell body enriched PI lipid class (Merrill et al., 2017) and synaptic lipid such as PA (Schwarz et al., 2011) and gangliosides (West et al., 2018). Dysregulated membrane phospholipid metabolism has been previously described to be associated with ER stress, which in turn triggers an increase in de novo synthesis of saturated phospholipids, including PIs and PAs (Shyu et al., 2019; Shank et al., 2001; Leamy et al., 2014). Likewise, gangliosides have been previously reported to increase their intracellular concentration under stressed conditions and activate ER stress as an adaptive response to cellular stress (d'Azzo et al., 2006). Indeed, one of the most striking features of areas that contain inclusions (CA1, CA3 and DG hippocampal subfields) in early symptomatic HD mice (12 weeks of age) was a reduction in lipid levels of species that serve as ER stress inhibitors. These include DHA-containing PS (44:12) and PG (44:12) (Begum et al., 2013), PI (Michell, 2018) and PE lipid classes (also referred to as 'lipid chaperones') (Patel and Witt, 2017; Trentzsch et al., 2020). We predict that the observed reduction in these lipids may impact ER-stress coping mechanisms in HD.

Such a mechanism is consistent with other studies finding ER stress as an early pathologic event in pre-symptomatic HD mice that persists (Carnemolla et al., 2009; Duennwald and Lindquist, 2008). Leitman et al. (2013) (Leitman et al., 2013) found ER stress was triggered in cultured cells with the expression of soluble and presumably oligomeric forms of mutant Httex1 before the appearance of visible aggregates. Also of note is a study by Lee (2012) (Lee et al., 2012), which reported that ER stress in HD mice is mediated by the activation of IRE1, which is also crucial for triggering a coordinated response that involves the upregulation of genes required for lipid biosynthesis to mitigate lipid bilayer stress (Strzyz, 2017; Travers et al., 2000; Ho et al., 2020). Therefore, these studies, along with our findings, are consistent with increased lipid synthesis in the early timepoint of HD (6 weeks of age), before the formation of inclusions, earmarking an adaptive response to ER stress.

Chronic activation of ER stress is known to trigger a cascade of neurotoxicity, leading to hippocampal synaptic dysfunction and memory loss (Sen, 2019), mitochondrial dysfunction (Malhotra and Kaufman, 2011), disrupted neurogenesis (Hood et al., 2018) and neuroinflammation (Sprenkle et al., 2017), subsequently contributing to poor neurological function and death in HD (Egger et al., 2007; Sano and Reed, 2013) (Fig. 8). Hence, the disturbances that we observed in lipid abundances in HD mice may contribute to chronic ER stress that has been previously linked to neuronal damage in both HD animal models (Shacham et al., 2019; Vidal et al., 2011) and post-mortem brain tissue from HD patients (Fazio et al., 2014; Jiang et al., 2016).

Even though the increase in lipid synthesis that we observed in HD mice appears to not support a general state of quiescence, it is well established that ER-stress mediated UPR activation is characterized by a shutdown of global protein synthesis except for proteins involved in protein folding (ER chaperones) and processing reactions to decrease the burden on ER (Paschen and Mengesdorf, 2005; Nakada et al., 2021). In particular, expression of pathogenic HTT was shown to induce ER-stress mediated phosphorylation of the alpha subunit of the eukaryotic initiation factor 2 (eIFα), which in turn led to a halt in general protein synthesis in a murine HD striatal cell line and striatum of transgenic HD mice (Leitman et al., 2014). These findings are in agreement with our previous in vitro study showing attenuation of protein translation in cells containing inclusions (Ramdzan et al., 2017), which is consistent with a state of ER stress in vivo.

The substantial increase in ^{2}H incorporation of PI lipid class that we observed across all the age groups, including pre-symptomatic HD mice is suggestive of different mechanisms at play to ER stress in early disease pathogenesis. PI lipid class directs the signaling of functions, including long-term potentiation (LTP) during synaptic plasticity (Dickson and Hille, 2019) and regulation of membrane trafficking and dynamics (Di Paolo and De Camilli, 2006). Moreover, the CA1 subfield, which mediates synaptic plasticity (Magó et al., 2020), displayed the highest number of PI lipid species with increased synthesis compared to the CA3 and DG subfields in HD mice. Consistent with this, previous studies have reported alterations in synaptic plasticity in hippocampal CA1 synapses at the early stages of HD (Murphy et al., 2000b; Quirion and Parsons, 2019). Indeed, a study by Ravalia et al. (2021) (Ravalia et al., 2021) has provided evidence for early impairment of synaptic plasticity and hippocampal deficits mediated by synaptic hyperexcitability in the CA1 stratum radiatum in pre-symptomatic HD mice, even before the onset of HD-like behavioural phenotype. Synaptic dysfunction has been considered a crucial pathological correlate, and likely causative agent, associated with cognitive decline in HD (Giralt et al., 2012a). Hence, disturbances in PI metabolism in the CA1 hippocampal subfield in pre-symptomatic HD mice (6 weeks of age) prior to the appearance of inclusions may signal the impairment of synaptic plasticity and contribute to cognitive impairment in HD mice, the onset of which typically occurs around 8–10 weeks of age.

The CA3 subfield showed particular changes in lipid profiles,

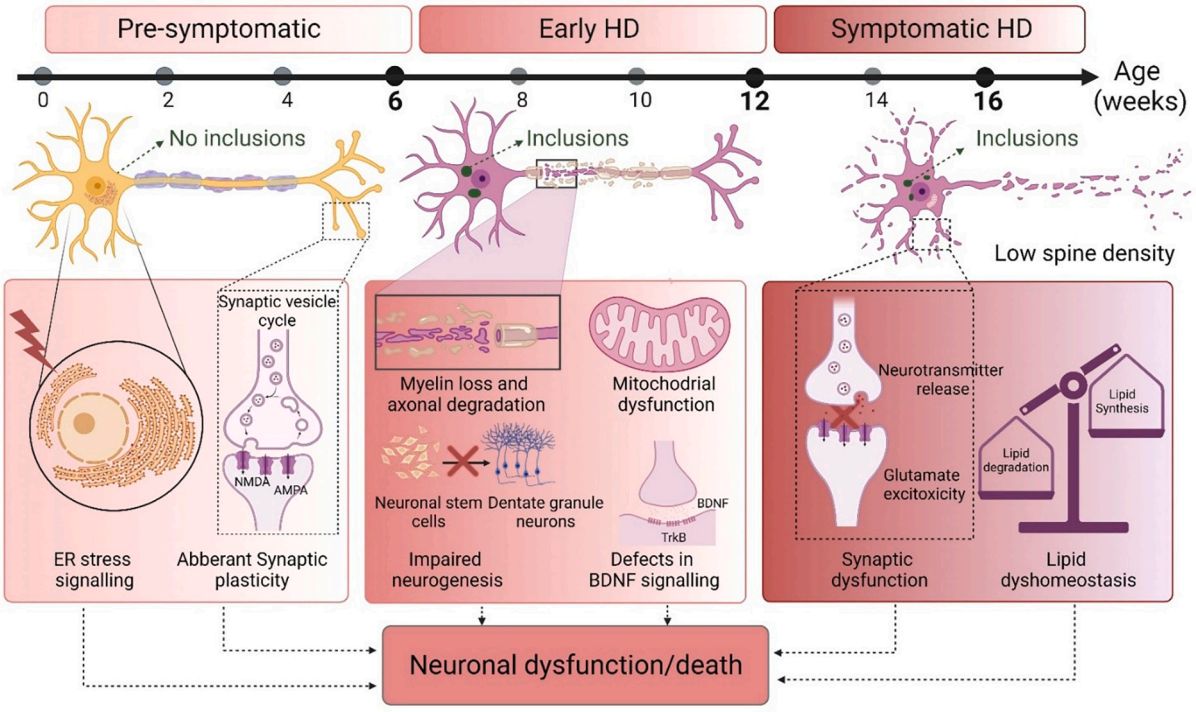

Fig. 8. Proposed model of the impact of aberrant lipid metabolism on neuronal dysfunction in HD mice. Possible mechanisms underlying neuronal dysfunction in HD based on the integration of steady-state and turnover analysis of neuronal lipids in the CA1, CA3 and DG hippocampal subfields in HD mice, both before and after inclusions manifest. Increased lipid synthesis in HD mice prior to the formation of inclusions (6 weeks of age) may signal ER stress and aberrant synaptic plasticity, processes that have been previously reported to be early pathological events in HD. By the time inclusions form, a pathological decline in lipid levels may trigger a cascade of neurotoxic events that influence key neuronal processes, including axonal degeneration, activation of brain-derived neurotrophic factor (BDNF), hippocampal neurogenesis, synaptic dysfunction and lipid homeostasis that may potentially contribute to cognitive impairment and neuronal dysfunction in HD mice. Figure created with BioRender.com.

particularly reduced abundances of the PG lipid class, at the earliest stages of HD we assessed (i.e., 6 weeks). PG is enriched in mitochondria (Chen et al., 2018a) and has been described to play a role in promoting neuronal survival under stress (Donoso et al., 2020). Mitochondrial defects have also been reported in pre-manifest HD carriers and pre-symptomatic HD mice (Panov et al., 2002; Lopes et al., 2022). Hence, the early downregulation of PG may correspond to a compromised ability of CA3 neurons to cope with stress during the early stages of HD before the onset of pathology or symptoms. By the time inclusions had formed (12 weeks of age), we observed the highest number of lipids showing reduced abundances in the CA3 hippocampal subfield at both the HD age groups that develop inclusions (12 and 16 weeks of age) compared to the CA1 and DG subfield, suggesting higher sensitivity of hippocampal CA3 subfield to lipid disturbances in HD mice. In support of this, prior studies have reported a higher sensitivity of the CA3 subfield to stress and neurodegeneration (Cherubini and Miles, 2015).

At the 12 and 16 weeks timepoints, the CA1 hippocampal sub-field of HD mice showed a striking reduction in the abundance of PE lipid class, which plays a crucial role in the activation of BDNF signaling (Che et al., 2020), a key regulator of synaptic (Lu et al., 2008) and mitochondrial plasticity (Chen et al., 2018b). Additionally, there was a striking loss of GM1, PS, PI lipid classes that have been shown to contribute to LTP and modulation of NMDA receptors, mechanisms that underlie hippocampal synaptic plasticity and associated learning and memory (Borghese, and Go'mez RA, Rami'rez OA., 1993; Bradley et al., 2017; Nolan et al., 2004; Fujii et al., 2002). Hence the reduced abundances of PE, PS, PI and GM1 in the CA1 subfield of 12- and 16-week-old HD mice may contribute to mechanisms implicated in onset of HD symptoms, including deficits in BDNF signaling (Zuccato et al., 2005), aberrant synaptic plasticity (Murphy et al., 2000b; Smith-Dijak et al., 2019) and mitochondrial dysfunction (Kim et al., 2010; Quintanilla and Johnson, 2009). In particular, the reduced abundance of the neuronal-specific DHA-containing PS (44:12) (Guo et al., 2007) in the CA1 subfield of 12-week-old HD mice may contribute to the loss of cognitive function and long-term memory in HD (Giralt et al., 2012a; Ransome et al., 2012b; Giralt et al., 2012b), as this lipid is known to play a significant role in improving memory and cognitive abilities in elderly subjects with mild cognitive impairments (Vakhapova et al., 2014; Yurko-Mauro et al., 2010). Furthermore, the reduced abundance of GM1 observed in the CA1 and CA3 subfield of 16-week-old HD mice may contribute to glutamate excitotoxicity reported in HD mice hippocampi (Sepers and Raymond, 2014), as exogenous addition of GM1 has been shown to enhance neuronal survival by providing protection from glutamate excitability in primary neuronal cultures (Favaron et al., 1988).

The dentate gyrus showed relatively fewer reductions in lipid abundances compared to CA1 and CA3 sub-fields in 12-week-old HD mice, with the most notable changes observed in the neuronal cell body-enriched PI and axonal-enriched PS lipid classes. PI has functions in regulating synaptic transmission, dendritic spine density (Dotti et al., 2014), membrane trafficking and dynamics, and signal transduction (Di Paolo and De Camilli, 2006), events that may contribute to enhanced hippocampal neurogenesis in the dentate gyrus. The other significantly impacted lipid class, PS, is involved in functions promoting adult hippocampal neurogenesis (Maragno et al., 2015), neuronal survival (Guo et al., 2007), and hippocampal-dependent cognitive performance (Babenko and YaA, 2011). Hence, the reduced levels of PI and PS in DG at 12 weeks of age may reflect impaired hippocampal neurogenesis reported earlier in HD (Gil-Mohapel et al., 2011). Yet another striking feature of the DG of 12-week-old HD mice was a significant reduction in the abundance of DHA-containing PG (44:12), which we have shown to be enriched in neuronal cell bodies. DHA-PG has been widely studied for its neuroprotective role (Crotty et al., 2008) in enhancing neuronal

survival through the activation of PI3-K/Akt pathway and increasing BDNF levels (Cole and Frautschy, 2010). Of note, previous work from our lab has reported impaired hippocampal neurogenesis mediated by reduced Akt signaling at the same age (12 weeks) in these R6/1 HD mice (Ransome and Hannan, 2013). Considering the emerging evidence highlighting the role of DHA in enhancing adult hippocampal neurogenesis (He et al., 2009) and the activation of Akt signaling pathway in promoting neurite growth and synaptogenesis (Akbar et al., 2005), we propose that DHA-PG (44:12) may serve as a marker of adult hippocampal neurogenesis.

A common feature that we observed at 16 weeks of age across all the three hippocampal subfields (CA1, CA3 and DG) in HD mice displaying inclusions was a significant reduction in relative abundances of synaptic lipids such as PA and PI, which have been implicated in synaptic vesicle cycling, neurotransmitter release (Puchkov and Haucke, 2013; Raben and Barber, 2017) and maintenance of lipid homeostasis (Ktistakis, 2010). These findings are in line with the existing evidence on the progressive decline in synaptic plasticity (Tyebji and Hannan, 2017; Quirion and Parsons, 2019), synaptic loss and lipid dyshomeostasis that may contribute to the onset and progression of hippocampal-dependent cognitive dysfunction in HD (Pardo and Maglione, 2018; Nithianantharajah et al., 2008). While our study focused on examining lipid changes in neuronal cell-body layers densely populated by intranuclear inclusions, given the well-established role of extranuclear (cytoplasmic and neuropril) aggregates on the alteration of synaptic function in HD (Li, 1999; Usdin et al., 1999; Benn et al., 2005; Li et al., 2000), we cannot rule out the contribution of the extranuclear aggregates present outside the neuronal cell body layers on synaptic changes in HD. We acknowledge that even though our cohort's sample size ($n = 6$/group, total = 72) was consistent with recent MSI studies (Hunter et al., 2018; Li et al., 2000), the power to detect any interactions between sex and genotype was not optimal. Secondly, even though our study targeted neuron-enriched hippocampal layers that display a two-fold higher neuronal density compared to glial cells (Carson et al., 2017), the spatial resolution of MALDI-imaging (30 μm) used in our study was insufficient to resolve glial cells from neurons. Considering that the diameter of each pyramidal neuron's cell body is 20–22 μm, the laser spot diameter of 30 μm used in the study most likely acquired spectra from a single neuron at a time. Nevertheless, to address the cellular heterogeneity within the hippocampal sub-fields, we categorized the detected lipids based on cell types, using a priori knowledge obtained from previously published cell type-specific lipidome of the mammalian brain, based on an extensive literature search (Table S3). Moreover, we were unable to determine whether the metabolic changes observed in our study emanated from intraneuronal or extraneuronal inclusions. Even though the proportion of glial cells containing aggregates is known to be much lower than neuronal cells (Osten and Margrie, 2013), glial aggregates have also been associated with neuronal excitotoxicity (Jansen et al., 2017; Shin et al., 2005) and synaptic dysfunction in HD (Tong et al., 2014) and may contribute to the observed metabolic changes associated with synaptic function in our study. Additionally, we have conducted MALDI-MSI in negative ionization mode, which limits the ability to observe permanent positively charged lipids such as PC and SM species. However, we were able to achieve a broad coverage of the most abundant brain lipids in the negative ionization mode.

5. Conclusion

Here, we demonstrated aberrant, and/or adaptive changes to lipid metabolism in the hippocampus of HD mice that were detected before inclusions and symptoms developed. We identified patterns of changes that evolved as pathology developed that map to key functions of ER stress, synaptic plasticity at the earliest pre-symptomatic stage of disease, which then extended to axonal degeneration, activation of brain-derived neurotrophic factor (BDNF), hippocampal neurogenesis, synaptic dysfunction and lipid homeostasis as inclusions formed in hippocampal neurons. We acknowledge that mutant huntingtin engages multiple pathogenic pathways and so the contribution of other lipid-independent mechanisms to the impairment of hippocampal function in HD cannot be excluded. Nevertheless, these findings provide new clues to the sequence of molecular events leading up to disease onset that may have potential for therapeutic targeting.

Supplementary data to this article can be found online at https://doi.org/10.1016/j.nbd.2022.105933.

Data and code availability statement

The raw data matrices (.csv files) and the paired *.ibd and *.imzML files have been deposited in Figshare at https://figshare.com/s/b026f2120f7ee98ca040. Additionally, the paired *.ibd and *.imzML files of the whole hippocampal region has also been made available at https://figshare.com/s/c5b9fa7e797266b31f2c for researchers interested in undertaking analysis of the other sub-regions within the HD mice hippocampi.

CRediT authorship contribution statement

Farheen Farzana: Writing – original draft, Formal analysis, Data curation, Software, Visualization. **Malcolm J. McConville:** Conceptualization, Methodology. **Thibault Renoir:** Methodology, Resources, Writing – review & editing. **Shanshan Li:** Investigation. **Shuai Nie:** Investigation, Writing – review & editing. **Harvey Tran:** Investigation. **Anthony J. Hannan:** Methodology, Resources, Writing – review & editing, Supervision, Project administration, Funding acquisition. **Danny M. Hatters:** Conceptualization, Writing – review & editing, Supervision, Project administration, Funding acquisition. **Berin A. Boughton:** Methodology, Validation, Writing – review & editing, Supervision, Project administration, Funding acquisition.

Declaration of Competing Interest

The authors declare no competing financial interests.

Data availability

Data will be made available on request.

Acknowledgements

We thank Federico Martinez-Seidel from Max Planck Institute of Molecular Plant Physiology, Germany for his technical help with the development of KineticMSI, an R-based data analysis pipeline. We also thank the Melbourne Mass Spectrometry and Proteomics Facility of The Bio21 Molecular Science and Biotechnology Institute and Metabolomics Australia at The University of Melbourne for mass spectrometry analysis. We also acknowledge the contribution of Melbourne Statistical Consulting Platform, University of Melbourne for their assistance with data analysis. For technical support with histology staining, we would like to thank Dr. Ian Birchall from the Histology and Neuropathology scientific services, Florey Institute of Neuroscience and Mental Health. This work was supported by National Health and Medical Research Council (NHMRC) through the Ideas Grant ID APP1184166 awarded to D Hatters, BA Boughton. D Hatters is an NHMRC Senior Research Fellow and AJ Hannan is an NHMRC Principal Research Fellow. The generation of the HD and WT mouse tissues was supported by Project Grant ID APP1124356 awarded to T Renoir and AJ Hannan. All authors contributed to the article and approved the final submitted version.

References

Akbar, M., Calderon, F., Wen, Z., Kim, H.Y., 2005. Docosahexaenoic acid: a positive modulator of Akt signaling in neuronal survival. Proc. Natl. Acad. Sci. 102 (31), 10858–10863.

Arrasate, M., Mitra, S., Schweitzer, E.S., Segal, M.R., Finkbeiner, S., 2004. Inclusion body formation reduces levels of mutant huntingtin and the risk of neuronal death. Nature. 431 (7010), 805–810.

Aufschnaiter, A., Kohler, V., Diessl, J., Peselj, C., Carmona-Gutierrez, D., Keller, W., et al., 2017. Mitochondrial lipids in neurodegeneration. Cell Tissue Res. 367 (1), 125–140.

Babenko, N.A., YaA, Semenova, 2011. Effects of exogenous phosphatidylserine on cognitive functions and phospholipid metabolism in the hippocampus of aged rats. Neurosci. Behav. Physiol. 41 (1), 97–101.

Begum, G., Harvey, L., Dixon, C.E., Sun, D., 2013 Dec. ER stress and effects of DHA as an ER stress inhibitor. Transl. Stroke Res. 4 (6), 635–642.

Benjamini, Y., Hochberg, Y., 1995. Controlling the false discovery rate: a practical and powerful approach to multiple testing. J. R. Stat. Soc. Ser. B Methodol. 57 (1), 289–300.

Benn, C.L., Landles, C., Li, H., Strand, A.D., Woodman, B., Sathasivam, K., et al., 2005. Contribution of nuclear and extranuclear polyQ to neurological phenotypes in mouse models of Huntington's disease. Hum. Mol. Genet. 14 (20), 3065–3078. Oct 15.

Blusztajn, J.K., Liscovitch, M., Mauron, C., Richardson, U.I., RJM, Wurtman, 1987. Phosphatidylcholine as a precursor of choline for acetylcholine synthesis. J. Neural Transm. Suppl. 24, 247–259.

Borghese, C.M., Go'mez RA, Rami'rez OA., 1993. Phosphatidylserine increases hippocampal synaptic efficacy. Brain Res. Bull. 31 (6), 697–700.

Bradley, R.M., Mardian, E.B., Bloemberg, D., Aristizabal Henao, J.J., Mitchell, A.S., Marvyn, P.M., et al., 2017. Mice deficient in lysophosphatidic acid acyltransferase delta (Lpaat δ)/ acylglycerophosphate acyltransferase 4 (Agpat4) have impaired learning and memory. Mol. Cell. Biol. 37 (22).

Brooks, S.P., Janghra, N., Workman, V.L., Bayram-Weston, Z., Jones, L., Dunnett, S.B., 2012. Longitudinal analysis of the behavioural phenotype in R6/1 (C57BL/6J) Huntington's disease transgenic mice. Brain Res. Bull. 88 (2–3), 94–103.

Cabanas, M., Piquemal, M., Pistono, C., Arnaud, S., Rakesh, D., Poinama, E., et al., 2020. Correlations between mutant huntingtin aggregates and behavioral changes in R6/1 mice. J. Huntingt. Dis. 9 (1), 33–45.

Carnemolla, A., Fossale, E., Agostoni, E., Michelazzi, S., Calligaris, R., De Maso, L., et al., 2009. Rrs1 is involved in endoplasmic reticulum stress response in Huntington disease. J. Biol. Chem. 284 (27), 18167–18173.

Carson, R.H., Lewis, C.R., Erickson, M.N., Zagieboylo, A.P., Naylor, B.C., Li, K.W., et al., 2017. Imaging regiospecific lipid turnover in mouse brain with desorption electrospray ionization mass spectrometry. J. Lipid Res. 58 (9), 1884–1892.

Che, H., Zhou, M., Zhang, T., Zhang, L., Ding, L., Yanagita, T., et al., 2018. Comparative study of the effects of phosphatidylcholine rich in DHA and EPA on Alzheimer's disease and the possible mechanisms in CHO-APP/PS1 cells and SAMP8 mice. Food Funct. 9 (1), 643–654.

Che, H., Zhang, L., Ding, L., Xie, W., Jiang, X., Xue, C., et al., 2020. EPA-enriched ethanolamine plasmalogen and EPA-enriched phosphatidylethanolamine enhance BDNF/TrkB/CREB signaling and inhibit neuronal apoptosis *in vitro* and *in vivo*. Food Funct. 11 (2), 1729–1739.

Chen, W.W., Chao, Y.J., Chang, W.H., Chan, J.F., Hsu, Y.H.H., 2018a. Phosphatidylglycerol incorporates into cardiolipin to improve mitochondrial activity and inhibits inflammation. Sci. Rep. 8 (1), 4919.

Chen, F., Danladi, J., Ardalan, M., Elfving, B., Müller, H.K., Wegener, G., et al., 2018b. A critical role of mitochondria in BDNF-associated synaptic plasticity after one-week vortioxetine treatment. Int. J. Neuropsychopharmacol. 21 (6), 603–615.

Cherubini, E., Miles, R., 2015. The CA3 region of the hippocampus: how is it? What is it for? How does it do it? Front. Cell. Neurosci. 9.

Cole, G.M., Frautschy, S.A., 2010. DHA may prevent age-related dementia. J. Nutr. 140 (4), 869–874.

Cole, L.K., Kim, J.H., Amoscato, A.A., Tyurina, Y.Y., Bayır, H., Karimi, B., et al., 2018. Aberrant cardiolipin metabolism is associated with cognitive deficiency and hippocampal alteration in tafazzin knockdown mice. Biochim. Biophys. Acta (BBA) - Mol. Basis Dis. 1864 (10), 3353–3367.

Colgan, S.M., Tang, D., Werstuck, G.H., Austin, R.C., 2007. Endoplasmic reticulum stress causes the activation of sterol regulatory element binding protein 2. Int. J. Biochem. Cell Biol. 39 (10), 1843–1851.

Crotty, S., Fitzgerald, P., Tuohy, E., Harris, D.M., Fisher, A., Mandel, A., et al., 2008. Neuroprotective effects of novel phosphatidylglycerol-based phospholipids in the 6-hydroxydopamine model of Parkinson's disease: neuroprotection in a model of Parkinson's disease. Eur. J. Neurosci. 27 (2), 294–300.

Davies, S.W., Turmaine, M., Cozens, B.A., DiFiglia, M., Sharp, A.H., Ross, C.A., et al., 1997. Formation of neuronal intranuclear inclusions underlies the neurological dysfunction in mice transgenic for the HD mutation. Cell. 90 (3), 537–548.

d'Azzo, A., Tessitore, A., Sano, R., 2006. Gangliosides as apoptotic signals in ER stress response. Cell Death Differ. 13 (3), 404–414.

de la Monte, S.M., Vonsattel, J.P., Richardson, E.P., 1988. Morphometric demonstration of atrophic changes in the cerebral cortex, white matter, and neostriatum in Huntington's disease. J. Neuropathol. Exp. Neurol. 47 (5), 516–525.

Denny, C.A., Desplats, P.A., Thomas, E.A., Seyfried, T.N., 2010. Cerebellar lipid differences between R6/1 transgenic mice and humans with Huntington's disease: cerebellar lipids in Huntington's disease. J. Neurochem. 115 (3), 748–758.

Desplats, P.A., Denny, C.A., Kass, K.E., Gilmartin, T., Head, S.R., Sutcliffe, J.G., et al., 2007. Glycolipid and ganglioside metabolism imbalances in Huntington's disease. Neurobiol. Dis. 27 (3), 265–277.

Di Paolo, G., De Camilli, P., 2006. Phosphoinositides in cell regulation and membrane dynamics. Nature. 443 (7112), 651–657.

Dickson, E.J., Hille, B., 2019. Understanding phosphoinositides: rare, dynamic, and essential membrane phospholipids. Biochem. J. 476 (1), 1–23.

DiFiglia, M., Sapp, E., Chase, K.O., Davies, S.W., Bates, G.P., Vonsattel, J.P., et al., 1997. Aggregation of Huntingtin in neuronal intranuclear inclusions and dystrophic neurites in brain. Science. 277 (5334), 1990–1993.

Dong, H.W., 2008. The Allen Reference Atlas: A Digital Color Brain Atlas of the C57Bl/6J Male Mouse, vol. ix. John Wiley & Sons Inc, Hoboken, NJ, US, 366 p. (The Allen reference atlas: A digital color brain atlas of the C57Bl/6J male mouse).

Donoso, F., Schverer, M., Rea, K., Pusceddu, M.M., Roy, B.L., Dinan, T.G., et al., 2020. Neurobiological effects of phospholipids in vitro: relevance to stress-related disorders. Neurobiol. Stress. 13, 100252.

Dotti, C.G., Esteban, J.A., Ledesma, M.D., 2014. Lipid dynamics at dendritic spines. Front. Neuroanat. 8.

Duennwald, M.L., Lindquist, S., 2008. Impaired ERAD and ER stress are early and specific events in polyglutamine toxicity. Genes Dev. 22 (23), 3308–3319.

Eckhardt, M., Hedayati, K.K., Pitsch, J., Lullmann-Rauch, R., Beck, H., Fewou, S.N., et al., 2007. Sulfatide storage in neurons causes hyperexcitability and axonal degeneration in a mouse model of metachromatic leukodystrophy. J. Neurosci. 27 (34), 9009–9021.

Egger, L., Madden, D.T., Rhême, C., Rao, R.V., Bredesen, D.E., 2007. Endoplasmic reticulum stress-induced cell death mediated by the proteasome. Cell Death Differ. 14 (6), 1172–1180.

Epand, R.M., 2017. Features of the phosphatidylinositol cycle and its role in signal transduction. J. Membr. Biol. 250 (4), 353–366.

Farzana, F., Martinez-Seidel, F., Hannan, A.J., Hatters, D., Boughton, B.A., 2022. KineticMSI, an R-Based Framework for Relative Quantification of Spatial Isotopic Incorporation in Mass Spectrometry Imaging Experiments. bioRxiv.

Favaron, M., Manev, H., Alho, H., Bertolino, M., Ferret, B., Guidotti, A., et al., 1988. Gangliosides prevent glutamate and kainate neurotoxicity in primary neuronal cultures of neonatal rat cerebellum and cortex. Proc. Natl. Acad. Sci. 85 (19), 7351–7355.

Fazio, E.N., Jiang, Y., Lajoie, P., 2014. Endoplasmic reticulum homeostasis in Huntington's disease. Austin J. Anat. 1 (5), 4.

Feng, C., Wang, H., Lu, N., Chen, T., He, H., Lu, Y., et al., 2014. Log-transformation and its implications for data analysis. Shanghai Arch. Psychiatry 26 (2), 105–109.

Fitzner, D., Bader, J.M., Penkert, H., Bergner, C.G., Su, M., Weil, T., et al., 2020. Cell-type- and brain-region-resolved mouse brain lipidome. Cell Rep. 17.

Fujii, S., Igarashi, K., Sasaki, H., Furuse, H., Ito, K., Kaneko, K., et al., 2002. Effects of the mono- and tetrasialogangliosides GM1 and GQ1b on ATP-induced long-term potentiation in hippocampal CA1 neurons. Glycobiology. 12 (5), 339–344.

Gaura, V., Lavisse, S., Payoux, P., Goldman, S., Verny, C., Krystkowiak, P., et al., 2017. Association between motor symptoms and brain metabolism in early Huntington disease. JAMA Neurol. 74 (9), 1088.

Gil-Mohapel, J., Simpson, J.M., Ghilan, M., Christie, B.R., 2011. Neurogenesis in Huntington's disease: can studying adult neurogenesis lead to the development of new therapeutic strategies? Brain Res. 1406, 84–105.

Gil-Mohapel, J., Brocardo, P., Christie, B., 2014. The role of oxidative stress in Huntington's disease: are antioxidants good therapeutic candidates? Curr. Drug Targets 15 (4), 454–468.

Giralt, A., Saavedra, A., Alberch, J., Pérez-Navarro, E., 2012a. Cognitive dysfunction in Huntington's disease: humans, mouse models and molecular mechanisms. J. Huntingt. Dis. 1 (2), 155–173.

Giralt, A., Puigdellivol, M., Carreton, O., Paoletti, P., Valero, J., Parra-Damas, A., et al., 2012b. Long-term memory deficits in Huntington's disease are associated with reduced CBP histone acetylase activity. Hum. Mol. Genet. 21 (6), 1203–1216.

Guo, M., Stockert, L., Akbar, M., Kim, H.Y., 2007. Neuronal specific increase of phosphatidylserine by docosahexaenoic acid. J. Mol. Neurosci. 33 (1), 67–73.

Halbleib, K., Pesek, K., Covino, R., Hofbauer, H.F., Wunnicke, D., Hänelt, I., et al., 2017. Activation of the unfolded protein response by lipid bilayer stress. Mol. Cell 67 (4), 673–684.e8.

Harris, K.L., Armstrong, M., Swain, R., Erzinclioglu, S., Das, T., Burgess, N., et al., 2019. Huntington's disease patients display progressive deficits in hippocampal-dependent cognition during a task of spatial memory. Cortex. 119, 417–427.

He, C., Qu, X., Cui, L., Wang, J., Kang, J.X., 2009. Improved spatial learning performance of fat-1 mice is associated with enhanced neurogenesis and neuritogenesis by docosahexaenoic acid. Proc. Natl. Acad. Sci. 106 (27), 11370–11375.

Ho, N., Xu, C., Thibault, G., 2018. From the unfolded protein response to metabolic diseases – lipids under the spotlight. J. Cell Sci. 131 (3) jcs199307.

Ho, N., Yap, W.S., Xu, J., Wu, H., Koh, J.H., Goh, W.W.B., et al., 2020. Stress sensor Ire1 deploys a divergent transcriptional program in response to lipid bilayer stress. J. Cell Biol. 219 (7) e201909165.

Hood, K.N., Zhao, J., Redell, J.B., Hylin, M.J., Harris, B., Perez, A., et al., 2018. Endoplasmic reticulum stress contributes to the loss of newborn hippocampal neurons after traumatic brain injury. J. Neurosci. 38 (9), 2372–2384.

Hunter, M., Demarais, N.J., Faull, R.L.M., Grey, A.C., Curtis, M.A., 2018. Subventricular zone lipidomic architecture loss in Huntington's disease. J. Neurochem. 146 (5), 613–630.

Hunter, M., Demarais, N.J., Faull, R.L.M., Grey, A.C., Curtis, M.A., 2021. An imaging mass spectrometry atlas of lipids in the human neurologically normal and Huntington's disease caudate nucleus. J. Neurochem. 157 (6), 2158–2172.

Iuliano, M., Seeley, C., Sapp, E., Jones, E.L., Martin, C., Li, X., et al., 2021. Disposition of proteins and lipids in synaptic membrane compartments is altered in Q175/Q7 Huntington's disease mouse striatum. Front. Synaptic Neurosci. 13, 12.

Jacquemyn, J., Cascalho, A., Goodchild, R.E., 2017. The ins and outs of endoplasmic reticulum-controlled lipid biosynthesis. EMBO Rep. 18 (11), 1905–1921.
Jansen, A.H.P., van Hal, M., Op den Kelder, I.C., Meier, R.T., de Ruiter, A., Schut, M.H., et al., 2017 Jan. Frequency of nuclear mutant huntingtin inclusion formation in neurons and glia is cell-type-specific. Glia. 65 (1), 50–61.
Jiang, Y., Chadwick, S.R., Lajoie, P., 2016. Endoplasmic reticulum stress: the cause and solution to Huntington's disease? Brain Res. 1648, 650–657.
Jin, J., Peng, Q., Hou, Z., Jiang, M., Wang, X., Langseth, A.J., et al., 2015. Early white matter abnormalities, progressive brain pathology and motor deficits in a novel knock-in mouse model of Huntington's disease. Hum. Mol. Genet. 24 (9), 2508–2527.
Johnson, W.E., Li, C., Rabinovic, A., 2007. Adjusting batch effects in microarray expression data using empirical Bayes methods. Biostatistics. 8 (1), 118–127.
Kaya, I., Michno, W., Brinet, D., Iacone, Y., Zanni, G., Blennow, K., et al., 2017. Histology-compatible MALDI mass spectrometry based imaging of neuronal lipids for subsequent immunofluorescent staining. Anal. Chem. 10.
Keller, D., Erö, C., Markram, H., 2018. Cell densities in the mouse brain: a systematic review. Front. Neuroanat. 12, 83.
Kim, J., Moody, J.P., Edgerly, C.K., Bordiuk, O.L., Cormier, K., Smith, K., et al., 2010. Mitochondrial loss, dysfunction and altered dynamics in Huntington's disease. Hum. Mol. Genet. 19 (20), 3919–3935.
Kim, J.Y., Garcia-Carbonell, R., Yamachika, S., Zhao, P., Dhar, D., Loomba, R., et al., 2018. ER stress drives lipogenesis and steatohepatitis via caspase-2 activation of S1P. Cell. 175 (1), 133–145.e15.
Kloehn, J., Saunders, E.C., O'Callaghan, S., Dagley, M.J., McConville, M.J., 2015. Characterization of metabolically quiescent leishmania parasites in murine lesions using heavy water labeling. Sacks DL, editor. PLoS Pathog. 11 (2) e1004683.
Ktistakis, N.T., 2010. Lipid signaling and homeostasis: PA- is better than PA-H, but what about those PIPs? Sci. Signal. 3 (151) pe46–pe46.
Kuczynski, B., Reo, N.V., 2006. Evidence that plasmalogen is protective against oxidative stress in the rat brain. Neurochem. Res. 31 (5), 639–656.
Lajoie, P., Snapp, E.L., 2010. Formation and toxicity of soluble polyglutamine oligomers in living cells. PLoS One 5 (12), e15245.
Lau, M.J., Nie, S., Yang, Q., Harshman, L.G., Mao, C., Williamson, N.A., et al., 2022. Lipid Metabolism of *Aedes aegypti* Females Following Blood Feeding Reveals Similar Changes in Functionally Related Lipids. bioRxiv.
Lazic, S.E., Grote, H., Armstrong, R.J.E., Blakemore, C., Hannan, A.J., van Dellen, A., et al., 2004. Decreased hippocampal cell proliferation in R6/1 Huntington's mice. Neuroreport. 15 (5), 811–813.
Leamy, A.K., Egnatchik, R.A., Shiota, M., Ivanova, P.T., Myers, D.S., Brown, H.A., et al., 2014. Enhanced synthesis of saturated phospholipids is associated with ER stress and lipotoxicity in palmitate treated hepatic cells. J. Lipid Res. 55 (7), 1478–1488.
Lee, H., Noh, J.Y., Oh, Y., Kim, Y., Chang, J.W., Chung, C.W., et al., 2012. IRE1 plays an essential role in ER stress-mediated aggregation of mutant huntingtin via the inhibition of autophagy flux. Hum. Mol. Genet. 21 (1), 101–114.
Leek, J.T., 2014. Svaseq: removing batch effects and other unwanted noise from sequencing data. Nucleic Acids Res. 42 (21), e161.
Leitman, J., Ulrich Hartl, F., Lederkremer, G.Z., 2013. Soluble forms of polyQ-expanded huntingtin rather than large aggregates cause endoplasmic reticulum stress. Nat. Commun. 4 (1), 2753.
Leitman, J., Barak, B., Benyair, R., Shenkman, M., Ashery, U., Hartl, F.U., et al., 2014. ER stress-induced eIF2-alpha phosphorylation underlies sensitivity of striatal neurons to pathogenic Huntingtin. Ryu H, editor. PLoS One 9 (3) e90803.
Li, H., 1999 Jul 1. Ultrastructural localization and progressive formation of neuropil aggregates in Huntington's disease transgenic mice. Hum. Mol. Genet. 8 (7), 1227–1236.
Li, J.Y., Conforti, L., 2013. Axonopathy in Huntington's disease. Exp. Neurol. 246, 62–71.
Li, H., Li, S.H., Johnston, H., Shelbourne, P.F., Li, X.J., 2000 Aug. Amino-terminal fragments of mutant huntingtin show selective accumulation in striatal neurons and synaptic toxicity. Nat. Genet. 25 (4), 385–389.
Li, H., Li, S.H., Yu, Z.X., Shelbourne, P., Li, X.J., 2001. Huntingtin aggregate-associated axonal degeneration is an early pathological event in Huntington's disease mice. J. Neurosci. 21 (21), 8473–8481.
Li, S., Ghosh, C., Xing, Y., Sun, Y., 2020. Phosphatidylinositol 4,5-bisphosphate in the control of membrane trafficking. Int. J. Biol. Sci. 16 (15), 2761–2774.
Lopes, C., Ferreira, I.L., Maranga, C., Beatriz, M., Mota, S.I., Sereno, J., et al., 2022. Mitochondrial and redox modifications in early stages of Huntington's disease. Redox Biol. 56, 102424.
Lu, Y., Christian, K., Lu, B., 2008. BDNF: a key regulator for protein synthesis-dependent LTP and long-term memory? Neurobiol. Learn. Mem. 89 (3), 312–323.
Lydic, T.A., Busik, J.V., Reid, G.E., 2014. A monophasic extraction strategy for the simultaneous lipidome analysis of polar and nonpolar retina lipids. J. Lipid Res. 55 (8), 1797–1809.
MacDonald, M.E., Ambrose, C.M., Duyao, M.P., Myers, R.H., Lin, C., Srinidhi, L., et al., 1993. A novel gene containing a trinucleotide repeat that is expanded and unstable on Huntington's disease chromosomes. Cell. 72 (6), 971–983.
Magaquian, D., Delgado Ocaña, S., Perez, C., Banchio, C., 2021. Phosphatidylcholine restores neuronal plasticity of neural stem cells under inflammatory stress. Sci. Rep. 11 (1), 22891.
Maglione, V., Marchi, P., Di Pardo, A., Lingrell, S., Horkey, M., Tidmarsh, E., et al., 2010. Impaired ganglioside metabolism in Huntington's disease and neuroprotective role of GM1. J. Neurosci. 30 (11), 4072–4080.
Magó, Á., Weber, J.P., Ujfalussy, B.B., Makara, J.K., 2020. Synaptic plasticity depends on the fine-scale input pattern in thin dendrites of CA1 pyramidal neurons. J. Neurosci. 40 (13), 2593–2605.
Malhotra, J.D., Kaufman, R.J., 2011. ER stress and its functional link to mitochondria: role in cell survival and death. Cold Spring Harb. Perspect. Biol. 3 (9) a004424.
Mangiarini, L., Sathasivam, K., Seller, M., Cozens, B., Harper, A., Hetherington, C., et al., 1996. Exon 1 of the HD gene with an expanded CAG repeat is sufficient to cause a progressive neurological phenotype in transgenic mice. Cell. 87 (3), 493–506.
Maragno, H., Rodella, P., da Silva Freitas, J., Fernando, Takase L., 2015. The effects of acute and chronic administration of phosphatidylserine on cell proliferation and survival in the dentate gyrus of adult and middle-aged rats. Brain Res. 1609, 72–81.
Mazurová, Y., Anderova, M., Němečková, I., Bezrouk, A., 2014. Transgenic rat model of Huntington's disease: a histopathological study and correlations with neurodegenerative process in the brain of HD patients. Biomed. Res. Int. 2014, 1–19.
Mehrotra, A., Sood, A., Sandhir, R., 2015. Mitochondrial modulators improve lipid composition and attenuate memory deficits in experimental model of Huntington's disease. Mol. Cell. Biochem. 410 (1–2), 281–292.
Merrill, C.B., Basit, A., Armirotti, A., Jia, Y., Gall, C.M., Lynch, G., et al., 2017. Patch clamp-assisted single neuron lipidomics. Sci. Rep. 7 (1), 5318.
Michell, R.H., 2018. Do inositol supplements enhance phosphatidylinositol supply and thus support endoplasmic reticulum function? Br. J. Nutr. 120 (3), 301–316.
Mo, C., Renoir, T., Pang, T.Y.C., Hannan, A.J., 2013. Short-term memory acquisition in female Huntington's disease mice is vulnerable to acute stress. Behav. Brain Res. 253, 318–322.
Molander-Melin, M., Pernber, Z., Franken, S., Gieselmann, V., Månsson, J.E., Fredman, P., 2004. Accumulation of sulfatide in neuronal and glial cells of arylsulfatase A deficient mice. J. Neurocytol. 33 (4), 417–427.
Murphy, K.P.S.J., Carter, R.J., Lione, L.A., Mangiarini, L., Mahal, A., Bates, G.P., et al., 2000a. Abnormal synaptic plasticity and impaired spatial cognition in mice transgenic for exon 1 of the human Huntington's disease mutation. J. Neurosci. 20 (13), 5115–5123.
Murphy, K.P.S.J., Carter, R.J., Lione, L.A., Mangiarini, L., Mahal, A., Bates, G.P., et al., 2000b. Abnormal synaptic plasticity and impaired spatial cognition in mice transgenic for exon 1 of the human Huntington's disease mutation. J. Neurosci. 20 (13), 5115–5123.
Nakada, E.M., Sun, R., Fujii, U., Martin, J.G., 2021. The impact of endoplasmic reticulum-associated protein modifications, folding and degradation on lung structure and function. Front. Physiol. 12, 665622.
Naver, B., Stub, C., Møller, M., Fenger, K., Hansen, A.K., Hasholt, L., et al., 2003. Molecular and behavioral analysis of the r6/1 huntington's disease transgenic mouse. Neuroscience. 122 (4), 1049–1057.
Neumann, E.K., Comi, T.J., Rubakhin, S.S., Sweedler, J.V., 2019 Apr 23. Lipid heterogeneity between astrocytes and neurons revealed with single cell MALDI MS supervised by immunocytochemical classification. Angew. Chem. Int. Ed. 58 (18), 5910–5914.
Nithianantharajah, J., Barkus, C., Murphy, M., Hannan, A.J., 2008. Gene–environment interactions modulating cognitive function and molecular correlates of synaptic plasticity in Huntington's disease transgenic mice. Neurobiol. Dis. 29 (3), 490–504.
Nolan, Y., Martin, D., Campbell, V.A., Lynch, M.A., 2004. Evidence of a protective effect of phosphatidylserine-containing liposomes on lipopolysaccharide-induced impairment of long-term potentiation in the rat hippocampus. J. Neuroimmunol. 151 (1–2), 12–23.
Osten, P., Margrie, T.W., 2013. Mapping brain circuitry with a light microscope. Nat. Methods 10 (6), 515–523.
Palavicini, J.P., Wang, C., Chen, L., Ahmar, S., Higuera, J.D., Dupree, J.L., et al., 2016. Novel molecular insights into the critical role of sulfatide in myelin maintenance/function. J. Neurochem. 139 (1), 40–54.
Panov, A.V., Gutekunst, C.A., Leavitt, B.R., Hayden, M.R., Burke, J.R., Strittmatter, W.J., et al., 2002. Early mitochondrial calcium defects in Huntington's disease are a direct effect of polyglutamines. Nat. Neurosci. 5 (8), 731–736.
Paoletti, L., Elena, C., Domizi, P., Banchio, C., 2011. Role of phosphatidylcholine during neuronal differentiation. IUBMB Life 63 (9), 714–720.
Pardo, A.D., Maglione, V., 2018. The S1P axis: new exciting route for treating Huntington's disease. Trends Pharmacol. Sci. 39 (5), 468–480.
Paschen, W., Mengesdorf, T., 2005. Endoplasmic reticulum stress response and neurodegeneration. Cell Calcium 38 (3–4), 409–415.
Patel, D., Witt, S.N., 2017. Ethanolamine and phosphatidylethanolamine: partners in health and disease. Oxidative Med. Cell. Longev. 2017, 1–18.
Paulsen, J.S., 2011. Cognitive impairment in Huntington disease: diagnosis and treatment. Curr. Neurol. Neurosci. Rep. 11 (5), 474–483.
Puchkov, D., Haucke, V., 2013. Greasing the synaptic vesicle cycle by membrane lipids. Trends Cell Biol. 23 (10), 493–503.
Quintanilla, R.A., Johnson, G.V.W., 2009. Role of mitochondrial dysfunction in the pathogenesis of Huntington's disease. Brain Res. Bull. 80 (4–5), 242–247.
Quirion, J.G., Parsons, M.P., 2019. The onset and progression of hippocampal synaptic plasticity deficits in the Q175FDN mouse model of Huntington disease. Front. Cell. Neurosci. 13.
Raben, D.M., Barber, C.N., 2017. Phosphatidic acid and neurotransmission. Adv. Biol. Regul. 63, 15–21.
Ramdzan, Y.M., Trubetskov, M.M., Ormsby, A.R., Newcombe, E.A., Sui, X., Tobin, M.J., et al., 2017. Huntingtin inclusions trigger cellular quiescence, deactivate apoptosis, and lead to delayed necrosis. Cell Rep. 19 (5), 919–927.
Ransome, M.I., Hannan, A.J., 2013. Impaired basal and running-induced hippocampal neurogenesis coincides with reduced Akt signaling in adult R6/1 HD mice. Mol. Cell. Neurosci. 54, 93–107.
Ransome, M.I., Renoir, T., Hannan, A.J., 2012a. Hippocampal neurogenesis, cognitive deficits and affective disorder in Huntington's disease. Neural Plast. 1–7.
Ransome, M.I., Renoir, T., Hannan, A.J., 2012b. Hippocampal neurogenesis, cognitive deficits and affective disorder in Huntington's disease. Neural Plast. 874387.

Rattray, I., Smith, E.J., Crum, W.R., Walker, T.A., Gale, R., Bates, G.P., et al., 2013. Correlations of behavioral deficits with brain pathology assessed through longitudinal MRI and histopathology in the R6/1 mouse model of Huntington's disease. Borchelt DR, editor. PLoS One 8 (12) e84726.
Ravalia, A.S., Lau, J., Barron, J.C., Purchase, S.L.M., Southwell, A.L., Hayden, M.R., et al., 2021. Super-resolution imaging reveals extrastriatal synaptic dysfunction in presymptomatic Huntington disease mice. Neurobiol. Dis. 152, 105293.
Romero, F., Hong, X., Shah, D., Kallen, C.B., Rosas, I., Guo, Z., et al., 2018. Lipid synthesis is required to resolve endoplasmic reticulum stress and limit fibrotic responses in the lung. Am. J. Respir. Cell Mol. Biol. 59 (2), 225–236.
Rosas, H.D., Koroshetz, W.J., Chen, Y.I., Skeuse, C., Vangel, M., Cudkowicz, M.E., et al., 2003. Evidence for more widespread cerebral pathology in early HD: an MRI-based morphometric analysis. Neurology. 60 (10), 1615–1620.
Sameni, S., Malacrida, L., Tan, Z., Digman, M.A., 2018. Alteration in fluidity of cell plasma membrane in Huntington disease revealed by spectral phasor analysis. Sci. Rep. 8 (1), 734.
Sano, R., Reed, J.C., 2013. ER stress-induced cell death mechanisms. Biochim. Biophys. Acta Mol. Cell Res. 1833 (12), 3460–3470.
Scherzinger, E., Sittler, A., Schweiger, K., Heiser, V., Lurz, R., Hasenbank, R., et al., 1999. Self-assembly of polyglutamine-containing huntingtin fragments into amyloid-like fibrils: implications for Huntington's disease pathology. Proc. Natl. Acad. Sci. 96 (8), 4604–4609.
Schwarz, K., Natarajan, S., Kassas, N., Vitale, N., Schmitz, F., 2011. The synaptic ribbon is a site of phosphatidic acid generation in ribbon synapses. J. Neurosci. 31 (44), 15996–16011.
Sen, N., 2019. ER stress, CREB, and memory: a tangled emerging link in disease. Neuroscientist. 25 (5), 420–433.
Sepers, M.D., Raymond, L.A., 2014. Mechanisms of synaptic dysfunction and excitotoxicity in Huntington's disease. Drug Discov. Today 19 (7), 990–996.
Shacham, T., Sharma, N., Lederkremer, G.Z., 2019. Protein misfolding and ER stress in Huntington's disease. Front. Mol. Biosci. 6, 20.
Shank, K.J., Su, P., Brglez, I., Boss, W.F., Dewey, R.E., Boston, R.S., 2001. Induction of lipid metabolic enzymes during the endoplasmic reticulum stress response in plants. Plant Physiol. 126 (1), 267–277.
Shin, J.Y., Fang, Z.H., Yu, Z.X., Wang, C.E., Li, S.H., Li, X.J., 2005 Dec 19. Expression of mutant huntingtin in glial cells contributes to neuronal excitotoxicity. J. Cell Biol. 171 (6), 1001–12.
Shyu, P., Ng, B.S.H., Ho, N., Chaw, R., Seah, Y.L., Marvalim, C., et al., 2019. Membrane phospholipid alteration causes chronic ER stress through early degradation of homeostatic ER-resident proteins. Sci. Rep. 9 (1), 8637.
Smith-Dijak, A.I., Sepers, M.D., Raymond, L.A., 2019. Alterations in synaptic function and plasticity in Huntington disease. J. Neurochem. 150 (4), 346–365.
Spires, T.L., Grote, H.E., Garry, S., Cordery, P.M., Dellen, A.V., Blakemore, C., et al., 2004. Dendritic spine pathology and deficits in experience-dependent dendritic plasticity in R6/1 Huntington's disease transgenic mice. Eur. J. Neurosci. 19 (10), 2799–2807.
Sprenkle, N.T., Sims, S.G., Sánchez, C.L., Meares, G.P., 2017. Endoplasmic reticulum stress and inflammation in the central nervous system. Mol. Neurodegener. 12.
Strzyz, P., 2017. Reacting to membrane stress. Nat. Rev. Mol. Cell Biol. 18 (8), 471–471.
Sugiura, Y., Shimma, S., Konishi, Y., Yamada, M.K., Setou, M., 2008. Imaging mass spectrometry technology and application on ganglioside study; visualization of age-dependent accumulation of C20-ganglioside molecular species in the mouse hippocampus. Astier Y, editor. PLoS One 3 (9) e3232.
Takahashi, T., Kikuchi, S., Katada, S., Nagai, Y., Nishizawa, M., Onodera, O., 2008. Soluble polyglutamine oligomers formed prior to inclusion body formation are cytotoxic. Hum. Mol. Genet. 17 (3), 345–356.
Takamori, S., Holt, M., Stenius, K., Lemke, E.A., Grønborg, M., Riedel, D., et al., 2006. Molecular anatomy of a trafficking organelle. Cell. 127 (4), 831–846.
Tanguy, E., Wang, Q., Moine, H., Vitale, N., 2019. Phosphatidic acid: from pleiotropic functions to neuronal pathology. Front. Cell. Neurosci. 13.
Tian, H., Sparvero, L.J., Blenkinsopp, P., Amoscato, A.A., Watkins, S.C., Bayır, H., et al., 2019. Secondary-ion mass spectrometry images cardiolipins and phosphatidylethanolamines at the subcellular level. Angew. Chem. Int. Ed. 58 (10), 3156–3161.
Tong, X., Ao, Y., Faas, G.C., Nwaobi, S.E., Xu, J., Haustein, M.D., et al., 2014 May. Astrocyte Kir4.1 ion channel deficits contribute to neuronal dysfunction in Huntington's disease model mice. Nat. Neurosci. 17 (5), 694–703.
Torkzaban, B., Mohseni Ahooyi, T., Duggan, M., Amini, S., Khalili, K., 2020. Crosstalk between lipid homeostasis and endoplasmic reticulum stress in neurodegeneration: insights for HIV-1 associated neurocognitive disorders (HAND). Neurochem. Int. 141, 104880.
Tracey, T.J., Steyn, F.J., Wolvetang, E.J., Ngo, S.T., 2018. Neuronal lipid metabolism: multiple pathways driving functional outcomes in health and disease. Front. Mol. Neurosci. 11, 10.
Travers, K.J., Patil, C.K., Wodicka, L., Lockhart, D.J., Weissman, J.S., Walter, P., 2000. Functional and genomic analyses reveal an essential coordination between the unfolded protein response and ER-associated degradation. Cell. 101 (3), 249–258.
Trentzsch, M., Nyamugenda, E., Miles, T.K., Griffin, H., Russell, S., Koss, B., et al., 2020. Delivery of phosphatidylethanolamine blunts stress in hepatoma cells exposed to elevated palmitate by targeting the endoplasmic reticulum. Cell Death Dis. 6 (1), 8.
Tsugawa, H., Cajka, T., Kind, T., Ma, Y., Higgins, B., Ikeda, K., et al., 2015. MS-DIAL: data-independent MS/MS deconvolution for comprehensive metabolome analysis. Nat. Methods 12 (6), 523–526.
Tyebji, S., Hannan, A.J., 2017. Synaptopathic mechanisms of neurodegeneration and dementia: insights from Huntington's disease. Prog. Neurobiol. 153, 18–45.
Usdin, M.T., Shelbourne, P.F., Myers, R.M., Madison, D.V., 1999 May 1. Impaired synaptic plasticity in mice carrying the Huntington's disease mutation. Hum. Mol. Genet. 8 (5), 839–846.
Vakhapova, V., Cohen, T., Richter, Y., Herzog, Y., Kam, Y., Korczyn, A.D., 2014. Phosphatidylserine containing omega-3 fatty acids may improve memory abilities in nondemented elderly individuals with memory complaints: results from an open-label extension study. Dement. Geriatr. Cogn. Disord. 38 (1–2), 39–45.
van Echten-Deckert, G., Herget, T., 2006. Sphingolipid metabolism in neural cells. Biochim. Biophys. Acta Biomembr. 1758 (12), 1978–1994.
Vidal, R., Caballero, B., Couve, A., Hetz, C., 2011. Converging pathways in the occurrence of endoplasmic reticulum (ER) stress in Huntington's disease. Curr. Mol. Med. 11 (1), 1–12.
Vodicka, P., Mo, S., Tousley, A., Green, K.M., Sapp, E., Iuliano, M., et al., 2015. Mass spectrometry analysis of wild-type and knock-in Q140/Q140 Huntington's disease mouse brains reveals changes in glycerophospholipids including alterations in phosphatidic acid and lyso-phosphatidic acid. J. Huntingt. Dis. 4 (2), 187–201.
Wang, T., Nie, S., Ma, G., Vlaminck, J., Geldhof, P., Williamson, N.A., et al., 2020. Quantitative lipidomic analysis of Ascaris suum. Cappello M, editor. PLoS Negl. Trop. Dis. 14 (12) e0008848.
Wanichthanarak, K., Jeamsripong, S., Pornputtapong, N., Khoomrung, S., 2019. Accounting for biological variation with linear mixed-effects modelling improves the quality of clinical metabolomics data. Comput. Struct. Biotech. J. 17, 611–618.
West, R.J.H., Briggs, L., Perona Fjeldstad, M., Ribchester, R.R., Sweeney, S.T., 2018. Sphingolipids regulate neuromuscular synapse structure and function in Drosophila. J. Comp. Neurol. 526 (13), 1995–2009.
Xie, Y.R., Castro, D.C., Bell, S.E., Rubakhin, S.S., Sweedler, J.V., 2020. Single-cell classification using mass spectrometry through interpretable machine learning. Anal. Chem. 92 (13), 9338–9347.
Xu, J., Taubert, S., 2021. Beyond proteostasis: lipid metabolism as a new player in ER homeostasis. Metabolites. 11 (1), 52.
Yang, C., Wang, X., Wang, J., Wang, X., Chen, W., Lu, N., et al., 2020. Rewiring neuronal glycerolipid metabolism determines the extent of axon regeneration. Neuron. 105 (2), 276–292.e5.
Yurko-Mauro, K., McCarthy, D., Rom, D., Nelson, E.B., Ryan, A.S., Blackwell, A., et al., 2010. Beneficial effects of docosahexaenoic acid on cognition in age-related cognitive decline. Alzheimers Dementia 6 (6), 456–464.
Zuccato, C., Liber, D., Ramos, C., Tarditi, A., Rigamonti, D., Tartari, M., et al., 2005. Progressive loss of BDNF in a mouse model of Huntington's disease and rescue by BDNF delivery. Pharmacol. Res. 52 (2), 133–139.